SABER Calibration and Measurement Algorithm Document (CMAD)

Table of Contents

1 Scope

This document describes the production of science data products from the Sounding of the Atmosphere using Broadband Emission Radiometry (SABER) instrument on the NASA Thermosphere-Ionosphere-Mesosphere Energetics and Dynamics (TIMED) satellite. This process began at the outset of the project (i.e., in 1991 upon development of the SABER proposal) when the SABER science and engineering teams deliberately chose to prioritize absolute radiometric calibration of the instrument [4,6]. This choice led to specific design approaches and parts selection that resulted in an accurate and long-lived instrument, now in its 20th year of routine, nominal operations [1].

The SABER project benefitted enormously from experience with prior spaceflight instruments, most notably the Limb Infrared Monitor of the Stratosphere (LIMS) instrument [101] that flew in 1978 on the Nimbus-VII satellite and the Halogen Occultation Experiment (HALOE) [121] that was launched in 1991 on the Upper Atmosphere Research Satellite (UARS). LIMS, being a thermal infrared emission sensor, is most closely related to SABER. The experience gained in radiometric calibration, radiative transfer calculation, and geophysical data product generation from these highly successful experiments was invaluable in guiding the development of SABER. In addition, investment by NASA in the development of expertise in non-local thermodynamic equilibrium (non-LTE) energetics and radiative transfer was essential to developing not only the SABER science algorithms but indeed the entire scope of the science provided by the instrument. This ultimately became a world-wide endeavor in measuring and understanding processes in collisional energy transfer between infrared active molecules and their environment necessary to quantify the extent of non-LTE effects. This understanding is essential to the extraction of accurate geophysical data from infrared radiances generated under non-LTE conditions. Research into and understanding of collisional energy transfer relative to infrared radiation in the mesosphere and thermosphere began in the mid-1980's and continues to this day.

2 Related Documentation

2.1 Applicable Documents

There are a variety of applicable documents relevant to this Calibration and Measurement Algorithm Document (CMAD) for SABER. These include formal project review documents (e.g., Preliminary Design Review, Critical Design Review, etc., documents), contract reports from the Space Dynamics Laboratory (SDL) that built and calibrated the SABER instrument under contract to the NASA Langley Research Center, documents from the Advanced Physics Lab (APL) at John Hopkins University,

and nearly one hundred peer-reviewed journal articles describing the SABER mission science, the SABER instrument, SABER algorithm requirements, needs for improved gas kinetic parameters, algorithm descriptions, data product accuracy and precisions, and data product inter-comparisons and validations. Table 1 provides information on important non-journal documents.

Table 1. SABER Related Documentation

Title	Document Number	Publication Date
TIMED General Instrument Interface Specification	APL 7363-9050	May 1998
TIMED Position and Attitude Geometry Description	APL SRS-98-157	August 1998
SABER Preliminary Design Review	SDL/96-067	December 1996
SABER Critical Design Review	SDL/97-076	October 1997
SABER Instrument Requirements Document	SDL/95-006, Revision B	April 1998
SABER System Acceptance Review	SDL/99-119	August 1999
SABER Instrument Specification Document	SDL/95-009, Revision 4	October 1999
SABER Ground Calibration Report	SDL/99-155	June 2000
SABER Operations Handbook	SDL/00-	December 2001

3 Overview and Background Information

3.1 Science Objectives

The overarching scientific objective of the SABER instrument is to conduct the first detailed, quantitative investigation of the thermal structure, dynamics, chemical composition, and energy balance of the Earth's mesosphere and lower thermosphere (MLT) region, nominally the region between 60 and 110 km. Long referred to as "the ignorosphere," this region is too high for routine measurement by aircraft

or balloon platforms and too low for in-situ measurements to be made from satellites. Suborbital rocket measurements only provide an occasional glimpse into this scientifically interesting region where critical dynamical processes span spatial scales from localized turbulent dissipation to planetary scale waves. The MLT system is forced from below by vertically propagating tides and waves and from above by the variability of the solar ultraviolet input and of the overall geospace environment.

3.2 SABER Instrument Description

3.2.1 SABER Measurement Concept

The SABER instrument (Figure 1) is a broadband radiometer with 10 detectors measuring Earth limb emission from 10 spectral bands, Table 2. The noise equivalent radiance (NER) values stated in the table are for the nominal detector temperature of 74 K that is maintained to typically within 0.2 K by a miniature cryogenic refrigerator.

Table 2. SABER channels.

Channel Number	Description	Filter 5% points (cm^{-1})	NER w/m^2 sr	Target Geophysical Parameters	Range (km)
1	Narrow 15 μm CO_2	649 - 698	2.57e-4	T(P), cooling	15-110
2	Wide 15 μm CO_2	581-764	3.07e-4	T(P), cooling	15-110
3	Wide 15 μm CO_2	580-763	3.28e-4	T(P), cooling	15-110
4	9.6 μm O_3	1015-1145	4.18e-4	O_3 VMR, cooling	15-100
5	6.3 μm H_2O	1369-1567	2.11e-5	H_2O VMR, cooling	15-90
6	5.3 μm NO	1865-1944	1.23e-6	cooling	100-300
7	4.3 μm CO_2	2303-2392	7.35e-7	CO_2 VMR, tracer	70-110
8	2.0 μm OH(υ)	4510-5152	1.21e-6	photochemistry	80-100
9	1.6 μm OH(υ)	5741-6414	3.37e-6	photochemistry	80-100
10	1.27 μm $O_2(1\Delta)$	7704-7969	2.51e-6	O_3 VMR, solar heating	50-100

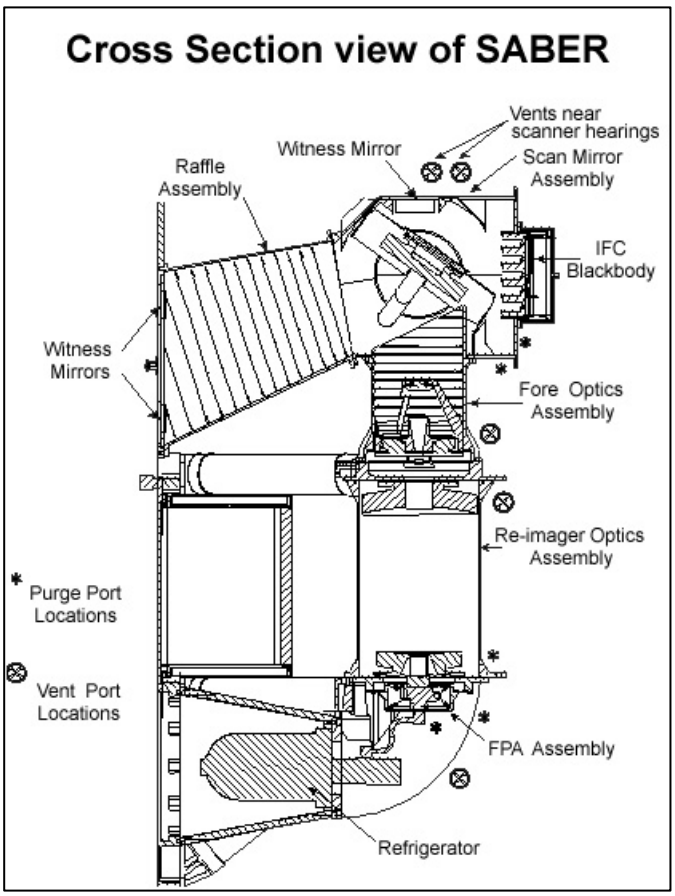

Figure 1. The SABER Instrument.

SABER takes its measurements from a circular Earth orbit inclined at 74.1˚ and at 625 km altitude. The orbit precesses 3˚ per day with respect to the Sun. The precessing orbit requires a yaw maneuver roughly every 60 days to prevent SABER from viewing the Sun. SABER views 90˚ clockwise or counterclockwise (depending on yaw mode) from the TIMED velocity vector so, due to its inclination, SABER measurements alternate between north viewing (latitude coverage of 83N to 52S) and south viewing (latitude coverage of 52N to 83S). Figure 2 shows the measurement tangent point track for a north viewing yaw mode. The TIMED orbital period is about 96 minutes thus the SABER measurement track circles the Earth 15 times per day. SABER performs about 49 up, down atmosphere scan sequences (98 full scans of the atmosphere) per orbital period. This is over 1400 scans per day for each of the 10 channels with a sampling rate that results in approximately 0.38 km spacing between samples for each scan.

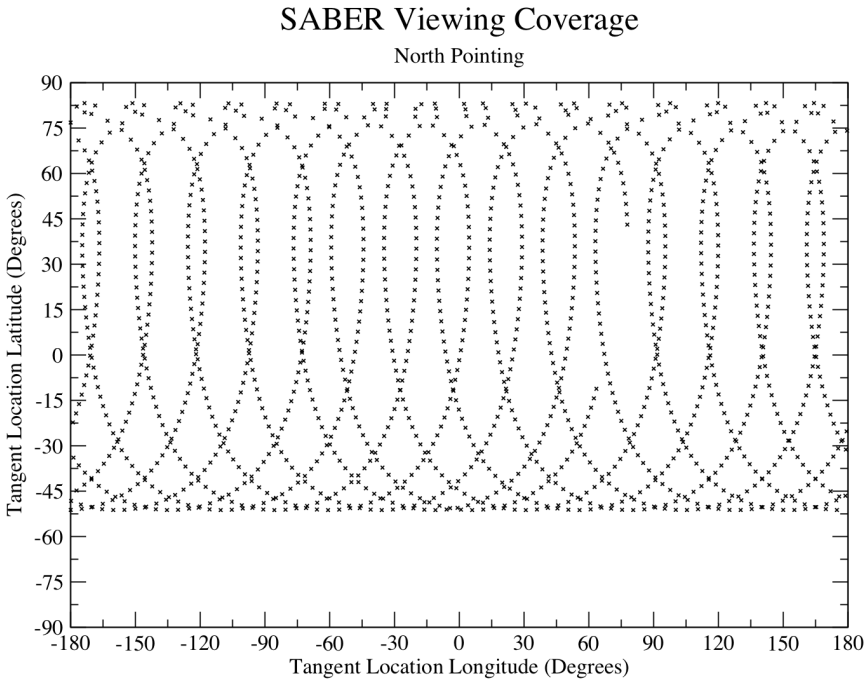

Figure 2. SABER tangent point track for a typical day during a north viewing yaw mode.

3.2.2 SABER Instrument Subsystem Description

The major SABER subsystems are:

1. Scanner assembly
2. Baffle assembly
3. Telescope assembly
4. IFC
5. FPA assembly
6. Instrument electronics
7. Refrigerator Assembly
8. Refrigerator Electronics
9. Spacecraft electrical interface

These major subsystems are shown in Figure 3 along with structural supports and radiators.

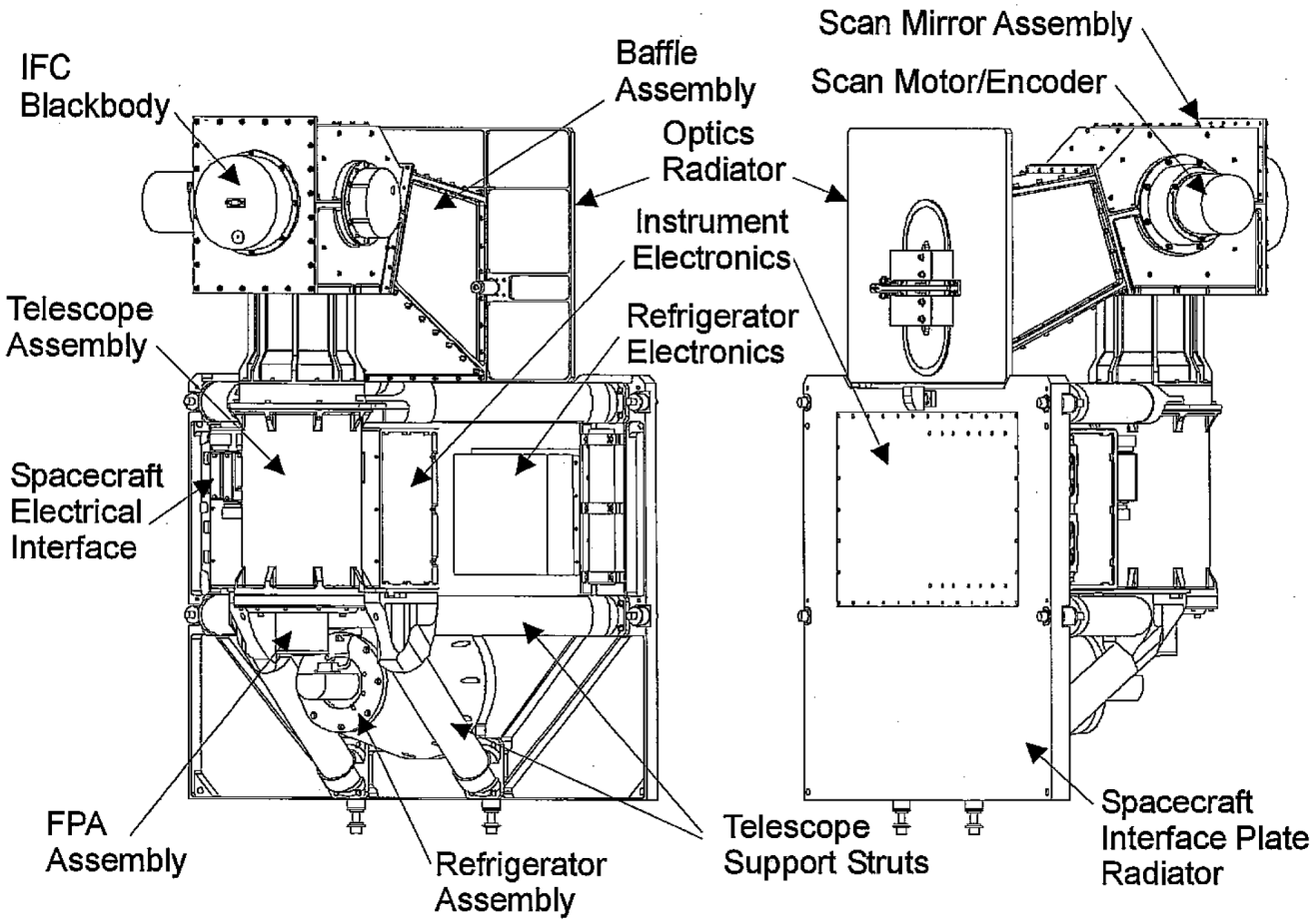

Figure 3. SABER instrument configuration.

3.2.3 SABER Heritage

3.2.3.1 SABER Instrument Heritage

The SABER investigation builds on extensive science and instrument heritage dating back to 1975 when Nimbus 6 was launched. The basic instrument technique of thermal emission limb sounding from LEO has been thoroughly demonstrated with LRIR [100], LIMS [101], and SAMS [115]. Several SABER science team members at the Langley Research Center were heavily involved in the highly successful LIMS experiment, including roles of Co-Team Leader or Co-Investigator.

In addition to the direct instrument heritage of LIMS, considerable technical expertise is possessed by members of the team at SDL/USU in the area of designing, building, testing, calibrating, and field support of infrared cryogenic payloads (interferometers and radiometers) on suborbital rockets, Space Shuttle pallets, and satellite platforms. This radiometric and cryogenic engineering expertise was built up over several years of high-altitude observations and scientific investigations of infrared emissions in polar

regions using rocket-borne platforms including HIRIS [123] and SPIRIT [93], providing a data base of infrared Earth limb auroral observations. SDL/USU team members were also responsible for the design, fabrication, testing, calibration, and field support of the very successful interferometer/radiometer CIRRIS [110] experiment flown on the Space Shuttle in 1991.

The SABER instrument design is based heavily on the LIMS instrument, employing the same limb acquisition and tracking system and nearly the same scan rate and IFOV as LIMS with a smaller telescope and simpler optics for higher throughput yielding enhanced S/N. The optical baffling is based on LIMS and SPIRIT experience but improved for better altitude coverage. A major difference is that SABER will use as a baseline design, a refrigerator detector cooling system for longer life, rather than a solid cryogen.

3.2.3.2 Algorithm and Calibration Heritage

The ability of thermal limb sounding to provide high vertical resolution and accurate temperature and composition results was confirmed by comparison of LIMS with rocket and balloon data [102][103][112][119][120]. The successful radiative transfer and retrieval techniques used for LIMS, which assume local thermodynamic equilibrium (LTE), are applied to the SABER measurements after modifications to account for emissions that are not in LTE (nonLTE). These techniques and extensions to nonLTE are discussed in section 5.1.1.

The SABER instrument has an operations-proven calibration heritage. The ability of SDL/USU and Langley Research Center to accurately calibrate optical filter and gas-filter IR radiometers has been demonstrated by the successful reduction of flight data from LIMS, HALOE [121], ERBE [94], CIRRIS, and SPIRIT. For SABER, techniques and technology developed by SDL/USU for CIRRIS and SPIRIT, and by NASA for LIMS and ERBE are applied, with particular emphasis on those from LIMS.

4 SABER Calibration Plan

4.1 Overall Calibration Scheme

Accurate limb-path emission measurements require detailed characterization of each channel including absolute response (counts to radiance), spectral response, field of view (FOV) response, electronic offsets, internal emission contributions, and internal flight calibrator source (IFC) characteristics. Detailed pre-launch calibration of the SABER instrument was performed by the Space Dynamic Laboratory (SDL) under NASA contract NAS1-20467 and reported in SDL/99-155. The pre-launch calibration is transferred to flight measurements by including measurement modes that remove offsets and provide continuous absolute response calibration. This is necessary because the instrument

state is constantly changing in response to the orbital environment, changes induced by active control of instrument temperature, and changes in temperature of the IFC and of the detectors. These measurement modes are accomplished on SABER by use of a scanning mirror that views the IFC and provides external view paths ranging from Earth surface to 500 km tangent altitude (space look), including paths through Earth's atmosphere from surface grazing to about 350km tangent altitude, Figure 4. The space view provides offset calibration while the IFC view provides absolute response calibration. The atmosphere scan mode is comprised of an up, down sequence in which the mirror first scans from Earth view to roughly 350km tangent altitude and then back down to Earth view and into the instrument baffle. This is repeated with a space look performed after every other up, down sequence and IFC calibration after every fourth.

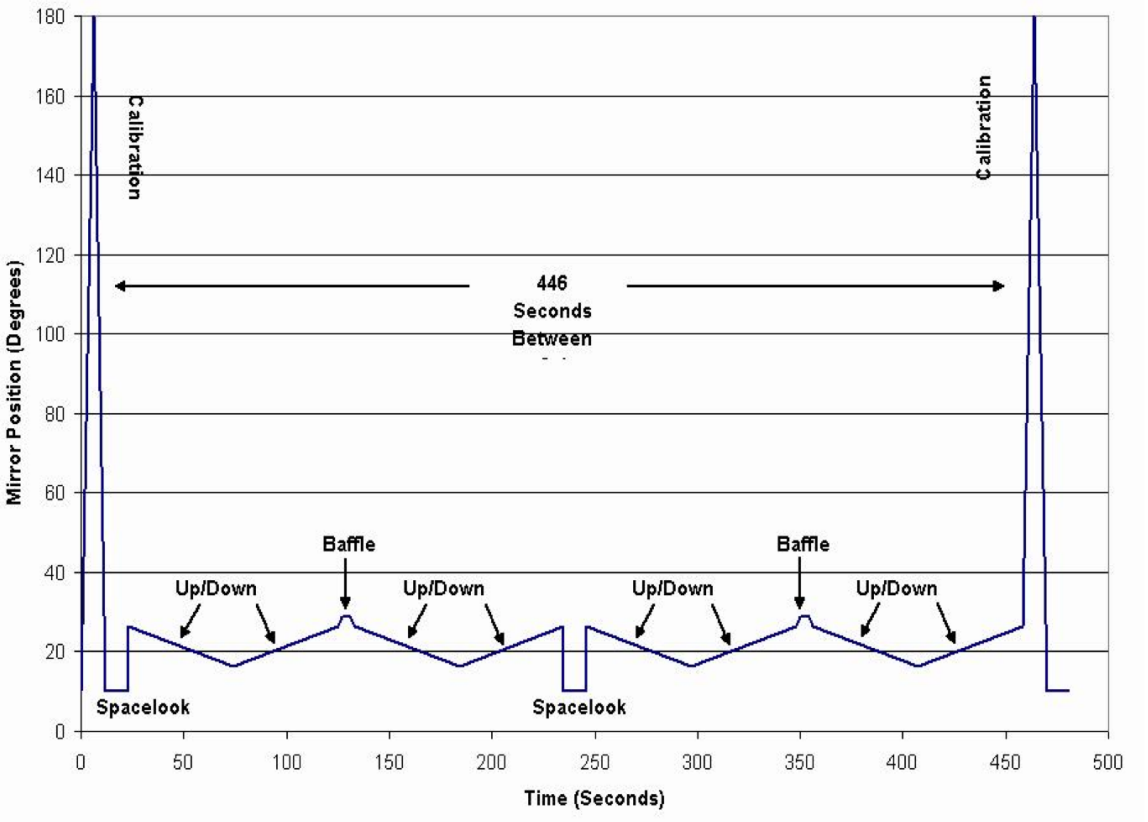

Figure 4. Mirror scan sequence.

4.2 Pre-flight Calibration Plan

The objective of SABER pre-flight calibration is to verify proper instrument operation, to estimate measurement uncertainties and to generate a specific calibration equation and radiometric model that relate the sensor output to the true flux. The calibration equation (1) is characterized in terms of separate radiometric parameters, which include offset, gain mode normalization, response linearity, off-axis extended source throughput correction and absolute responsivity.

$$L_m = \frac{1}{R_{ch}} r_{c,ch} = \frac{1}{R_{ch}} \left[Y_{ch,i}(Scn) L_{ch,i} \left(G_{ch,i} \left(r_{ch,i} - O_{ch,i} \right) \right) \right] \quad (1)$$

where L_m is measured radiance, R_{ch} is peak radiance responsivity, $r_{c,ch}$ is corrected instrument response, $Y_{ch,i}(\ )$ is off-axis extended source throughput correction, Scn is scan mirror pointing angle, $G_{ch,i}$ is gain mode normalization, $L_{ch,i}$ is linearity correction, $r_{ch,i}$ is detector response, $O_{ch,i}$ is sensor offset, ch is channel number, and i is gain mode. The goal of the pre-flight calibration is to characterize the parameters on the right-hand side of equation (1) over the range of expected on-orbit environmental conditions. The approaches taken by SDL to achieve this, and the results of that effort are discussed in detail in the SABER ground calibration report SDL/99-155 and summarized in [3].

4.2.1 SABER Pre-flight calibrations

The parameters on the right side of equation (1) were thoroughly characterized and calibrated as discussed in SDL/99-155. This was accomplished by using the completed SABER instrument as a radiometer with calibrations performed for each channel to fully characterize relative spectral response (RSR), instantaneous field-of-view (IFOV), absolute response, noise equivalent radiance (NER), internal scattering, signal offset, gain mode ratios, and other important characteristics of the instrument. Some of these characterizations are discussed in the following subsections.

4.2.1.1 RSR

The relative spectral responsivity (RSR) is the peak normalized responsivity at different wavelengths both inside and outside the band of each channel. Table 3 list the measured in-band and Table 4 the out-of-band characteristics and specifications for all 10 channels. Measured values are within required margin for all channels except channel 1 which has approximately 4 times the out of band

requirement, which may have some small impact on retrieved T(P). On-orbit performance has found that channels 4 and 5 may also have significant OOB contributions.

Table 3. In-band performance for SABER channels.

Channel Number and Species		Center Wavenumber (Wavelength) (cm^{-1})		Spectral Bandpass (cm^{-1})		5% Relative Transmittance Limits (cm^{-1})	
		Spec.	Meas.	Spec.	Meas.	Spec.	Meas.
1	CO_2 (N)	673	674	45	49	695 - 650	698 - 649
2	CO_2 (W)	670	672	180	183	760 - 580	763 - 580
3	CO_2 (W)	670	671	180	184	760 - 580	763 - 579
4	O_3	1075	1080	130	133	1140 - 1010	1146 - 1013
5	H_2O	1470	1468	180	199	1560 - 1380	1567 - 1368
6	NO	1895	1904	65	82	1930 - 1865	1945 - 1863
7	CO_2	2360	2348	80	89	2400 - 2320	2392 - 2303
8	OH (A)	4850	4833	700	648	5200 - 4500	5157 - 4509
9	OH (B)	6088	6079	695	675	6435 - 5740	6416 - 5741
10	O_2	7850	7837	240	268	7970 - 7730	7971 - 7703

Table 4. Out-of-band performance for SABER channels.

Channel Number and Species		Out-of-Band Rejection Ratio (relative to peak in-band response)	
		Req.	Meas.
1	CO2 (N)	< 10-4	< 4x10-4
2	CO2 (W)	< 10-3	< 10-4
3	CO2 (W)	< 10-3	< 10-4
4	O3	< 5x10-4	< 3x10-4
5	H2O	< 10-4	< 10-4
6	NO	< 10-4	< 10-5
7	CO2	< 10-4	< 10-4
8	OH (A)	< 10-4	< 10-4
9	OH (B)	< 10-4	< 1.9x10-4
10	O2	< 10-4	< 10-4

4.2.1.2 IFOV

The SABER instrument instantaneous FOV (IFOV) requirement is 2 km full-width at half-maximum (FWHM) at 60 km earth limb tangent height. Angular results obtained from these measurements were converted to tangent height altitude in units of km assuming a 6367-km earth radius and a 625-km orbital altitude. A blackbody located behind a small slit aperture at the focus of the full field collimator was used to simulate SABER's point response. A total of 31 cross-scan positions with a range of ± 15 mrad and a resolution of 1 mrad were obtained for each IFOV measurement.

The IFOV data were used to generate in-scan and cross-scan IFOV intensity profiles for each detector on the focal plane. Figure 5 shows the detector positions on the focal plane array (FPA) and responses as a function of angle for the FPA center viewing the 60 km tangent point. Data from the IFOV collection procedure were background, gain mode, linearity, and low-pass filter corrected before being summarized and plotted.

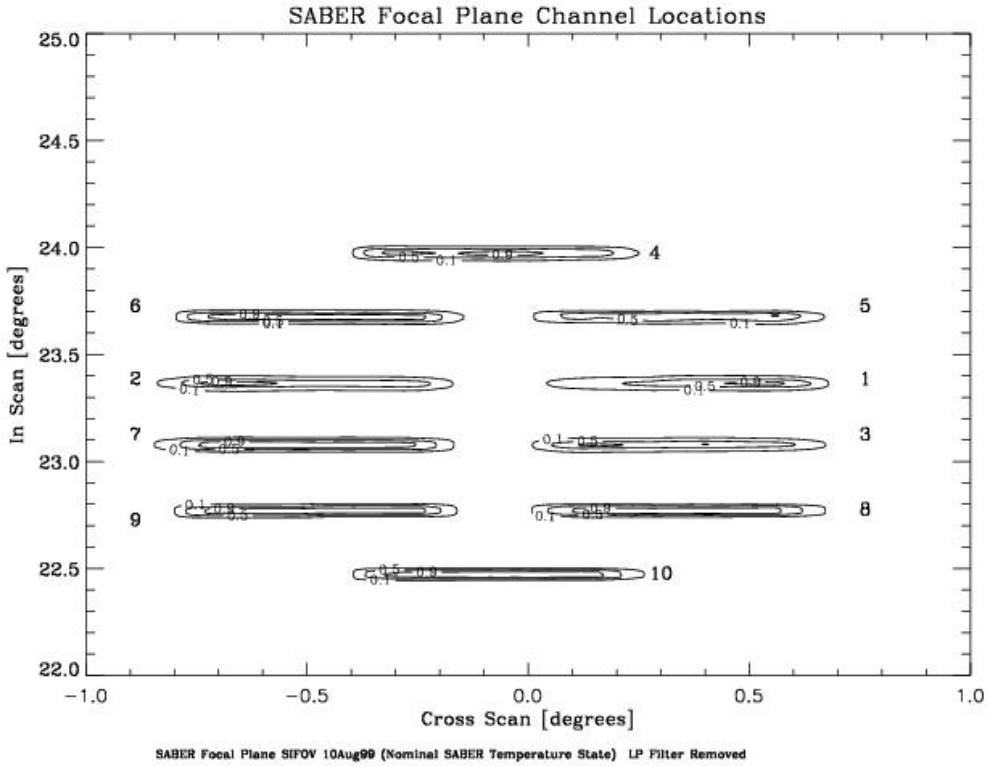

Figure 5. 60 km static IFOV: 10, 50 and 90 percent response contour lines shown for each channel.

The Full-Width Half-Max (FWHM) of the IFOV for each channel was determined by calculating the mean IFOV response for up and down scans together and determining the width of the central lobe at half the peak value. The resulting FWHM for each channel at 60km tangent height is listed in Table 5. For most of the channels, the FWHM are less than or very close to the 2 km requirement, channels 4,6 and 7 have a field of view slightly greater than 2.1 km at 60 km.

Table 5. IFOV for SABER channels.

Channel #	FWHM IFOV		Uncertainty
	degrees	km, at 60 km tangent height	km, at 60 km tangent height
1	0.040	1.94	0.083
2	0.040	1.94	0.078
3	0.041	1.96	0.084
4	0.043	2.13	0.064
5	0.040	1.96	0.066
6	0.043	2.11	0.070
7	0.044	2.11	0.063
8	0.043	2.03	0.061
9	0.043	2.03	0.068
10	0.042	1.96	0.066

In determining extended IFOV it is important to characterize near angle scatter (NAS). NAS occurs when signals are registered from regions that are outside the nominal field of view for that channel and can result from electrical crosstalk and/or optical scatter mechanisms. NAS signals can be observed in the log-scale static IFOV plots shown in Figure 6. Channel crosstalk occurs when a signal registers on a channel when another channel is being illuminated. This can occur through electronic means within the signal path, or by optical means when energy is scattered from the illuminated channel and is intercepted by another channel. In the plots shown in Figure 6, crosstalk is evident as channel response away from the IFOV central lobe, corresponding to the location of another channel. For example, the IFOV response curve for channel 2 shows crosstalk in the location of channel 4. Channel crosstalk is less than 1% for all SABER channels.

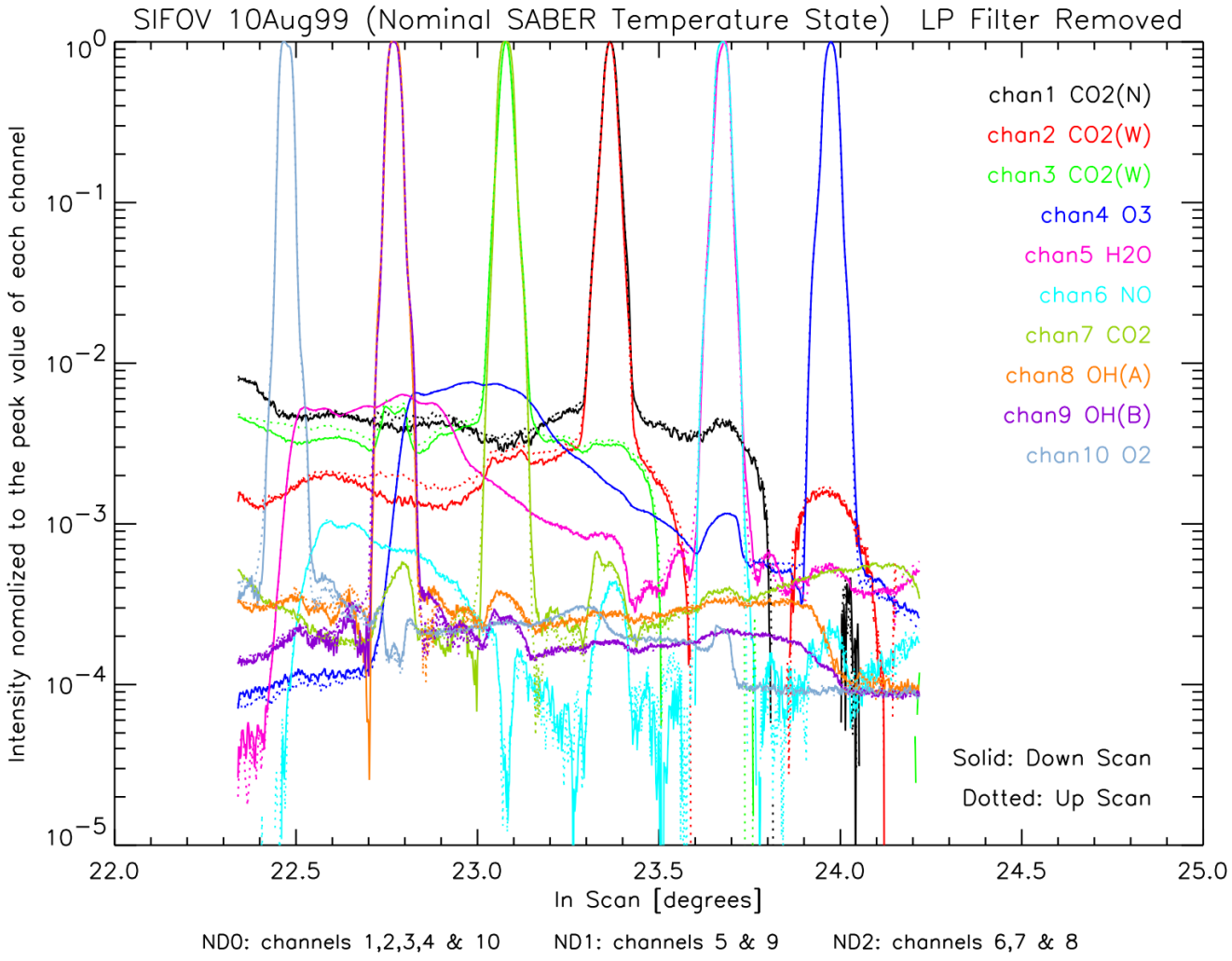

Figure 6. Extended off-axis response for each channel.

Note that from the first day of on-orbit data analysis it was realized that the laboratory data was only usable in the vicinity of the main FOV lobe and first side lobe (and for some channels the second side lobe). The remainder of the FOV functions were not adequately characterized during ground calibration. For example, Figure 7 shows laboratory and the current on-orbit derived FOV curves for channel 1. The laboratory curves were first corrected using a sequence of lunar scans that helped define the wings of the FOV function. That data resulted in much better defined FOV functions past the first side lobe. Due to limitations of that procedure, the functions past about 1 degree from center were still not well characterized, and the FOV functions were extended out to 2.5 degrees from center using a function

estimated from BRDF curves for the scan mirror. The red dashed curve in Figure 7 is the final corrected curve used for v2.0 analysis.

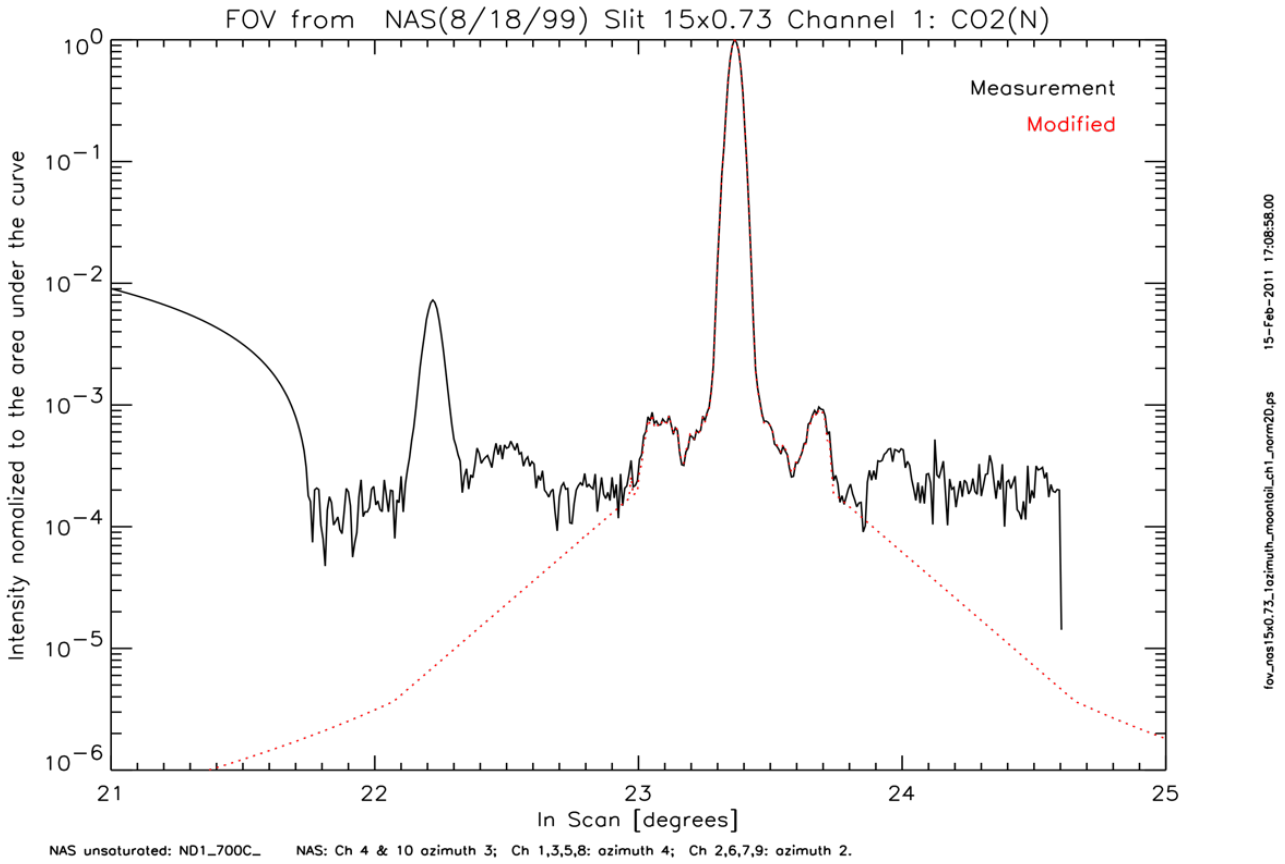

Figure 7. SABER FOV functions for channel 1, solid black is the laboratory calibration curve and dashed red is the curve used in the v2.0 algorithm.

4.2.1.3 Absolute Response

Low and high temperature blackbody (LTBB and HTBB) test were used to characterize the IFC and the absolute radiometric response, NER, and linearity for each channel. The radiance responsivity and the curve fit standard error for each channel and instrument temperature state is given in Table 6, which also shows the average and standard deviation for all temperature states. Because the hot focal plane temperature state clearly reduces responsivity on some channels, it was not included in the average or standard deviation calculation.

Table 6. Peak radiance responsivity for each SABER temperature state.

Channel	Responsivity													
	Temperature State[a]												Average [Counts per W/(cm^2 *sr)	Standard deviation [Counts per W/(cm^2 *sr)
	N, N, N		N, H, N[b]		N, N, C		N, N, H		C, N, N		H, N, N			
	Value [Counts per W/(cm^2 *sr)	Standard error [%]	Value [Counts per W/(cm^2 *sr)	Standard error [%]	Value [Counts per W/(cm^2 *sr)	Standard error [%]	Value [Counts per W/(cm^2 *sr)	Standard error [%]	Value [Counts per W/(cm^2 *sr)	Standard error [%]	Value [Counts per W/(cm^2 *sr)	Standard error [%]		
1	1.10e+08	0.04	7.79e+07	0.05	1.12e+08	0.16	1.14e+08	0.04	1.10e+08	0.01	1.10e+08	0.02	1.11e+08	1.53e+06
2	1.05e+08	0.06	7.50e+07	0.07	1.07e+08	0.13	1.08e+08	0.07	1.06e+08	0.04	1.06e+08	0.03	1.06e+08	1.31e+06
3	9.40e+07	0.09	6.55e+07	0.08	9.59e+07	0.15	9.72e+07	0.10	9.42e+07	0.06	9.50e+07	0.05	9.53e+07	1.31e+06
4	8.55e+08	0.34	8.62e+08	0.48	8.49e+08	0.32	8.56e+08	0.44	8.53e+08	0.36	8.48e+08	0.34	8.52e+08	3.60e+06
5	1.38e+09	0.34	1.43e+09	0.47	1.37e+09	0.32	1.38e+09	0.46	1.38e+09	0.37	1.37e+09	0.31	1.38e+09	5.85e+06
6	2.15e+10	0.03	2.15e+10	0.05	2.13e+10	0.02	2.15e+10	0.04	2.15e+10	0.05	2.14e+10	0.03	2.14e+10	8.70e+07
7	2.64e+10	0.03	2.64e+10	0.04	2.60e+10	0.04	2.63e+10	0.06	2.64e+10	0.03	2.54e+10	0.03	2.61e+10	4.22e+08
8	1.65e+10	0.14	1.64e+10	0.11	1.63e+10	0.07	1.63e+10	0.02	0.00e+00	NA[c]	0.00e+00	NA[c]	1.63e+10	1.02e+08
9	7.97e+09	0.18	7.94e+09	0.23	7.89e+09	0.21	7.95e+09	0.23	0.00e+00	NA	0.00e+00	NA	7.94e+09	3.87e+07
10	9.03e+09	0.04	8.92e+09	0.02	8.93e+09	0.06	8.93e+09	0.03	0.00e+00	NA	0.00e+00	NA	8.97e+09	5.90e+

a. Telescope, focal plane, baseplate temperature state. C=cold, N=nominal, and H=hot
b. Not used for average and standard deviation calculation over all temperature states
c. HTBB measurements were not obtained in this temperature state

IFC blackbody (IFCBB) emissivity were determined using the IFCBB measurements at 247.6K and the LTBB measurements at around 247.6 K. The list of emissivity for each channel is given in Table 7.

Table 7. IFC emissivity.

Channel	1	2	3	4	5	6	7
Emissivity	0.998	0.997	0.997	0.995	0.997	0.996	0.995

Data from the LTBB and the HTBB were also used to provide a radiometric verification of gain mode normalization values determined from electronic subsystem testing. Certain blackbody temperatures

and attenuating plate combinations were chosen to give good signal-to-noise for each gain setting at each instrument temperature state. Gain values determined from the electronic subsystem tests and from the blackbody tests for nominal instrument temperature are summarized in Table 8. The high gain-mode normalization values are set equal to 1. The gain-mode normalization values for the low and medium gain settings were calculated by dividing the high gain slope coefficient by the low and medium gain slope coefficients, respectively.

Table 8. Gain-mode normalization for each SABER channel.

Channel	High G	Medium G			Low G		
		Elec.	*BB*	*%diff*	*Elec.*	*BB*	*%diff*
1	1.000	1.000	1.0	0	21.114	21.1	0
2	1.000	7.816	7.8	0	60.103	60.5	0.7
3	1.000	8.318	8.3	0	68.858	69.2	0.4
4	1.000	13.454	13.4	-0.7	183.558	189.4	3.2
5	1.000	12.547	12.6	0.8	152.916	149	-2.6
6	1.000	19.157	19.2	0	209.571	211.5	0.9
7	1.000	8.647	8.6	0	76.758	76.5	-0.4
8	1.000	33.552	33.6	0	1108.443	1106.7	-0.2
9	1.000	32.730	32.7	0	1080.965	1130.2	4.6
10	1.000	19.198	19.1	-0.5	375.434	376.8	0.4

4.2.2 SABER Instrument Description

Figure 8 shows the SABER instrument functional design [4]. SABER uses a Cassegrain telescope design with a picket-fence tuning fork chopper at the first focus, and a clamshell re-imager to focus the image on the focal plane. The optical design consists of a high off-axis rejection telescope, a single axis scan mirror, a chopper, filters and 10 detector focal plane elements. The telescope was designed to reject stray light from the Earth and atmosphere outside the instrument instantaneous field-of-view (IFOV). The baffle assembly contains a single axis scan mirror which permits the 2 km vertical IFOV of each detector to be scanned across the limb from the Earth surface to a 350 km tangent height to produce vertical spectral

radiance profiles of the stratosphere, mesosphere and lower thermosphere. The scan mirror velocity and detector sample rate give five vertical earth limb samples per detector IFOV. The angular range of the scan mirror is approximately 16°, which allows SABER to look from cold space down to hard Earth. Accurate vertical registration of the tangent height of the data in the atmosphere is achieved by analysis of the 15 μm CO_2 channels.

The detector focal plane assembly, consisting of a filter array, a detector array, and a Lyot stop is cooled to 74 K by a miniature cryogenic refrigerator. The SABER detector array contains discrete HgCdTe, InSb, and InGaAs detectors. Each detector has an instantaneous field of view (IFOV) of 0.7 mrad by 10 mrad. The 0.7 mrad angular detector width gives a vertical footprint on the earth limb of approximately 2 km for a 60 km tangent height look angle and a 600 km orbit. The focal length of the telescope is 200 mm with f-number 2. Each detector or channel is spectrally filtered to a unique passband. The electrical signal from each of the 10 channels is pre-amplified and coherently rectified using phase-lock amplifiers synchronized with the chopper. Each channel contains a 12-bit analogue-to-digital converter. All 10 channels have multiple gain settings. The instrument contains In-Flight Calibration (IFC) radiation sources to confirm or update sensor calibration during on-orbit operations.

The IFC is comprised of a blackbody operating at ~248 K and 3 Jones sources. Long term radiometric stability of SABER is dependent on drifts in the emissivity of the blackbody, temperature sensor stability, and stability of the Jones sources. Since TIMED has extended far past its original 2-year mission and since SABER currently provides 20+ years of data for study of long-term trends, it is important to monitor stability of its radiometric calibration. As discussed in section 4.4, SABER has exhibited remarkable radiometric stability over its 20+ year mission.

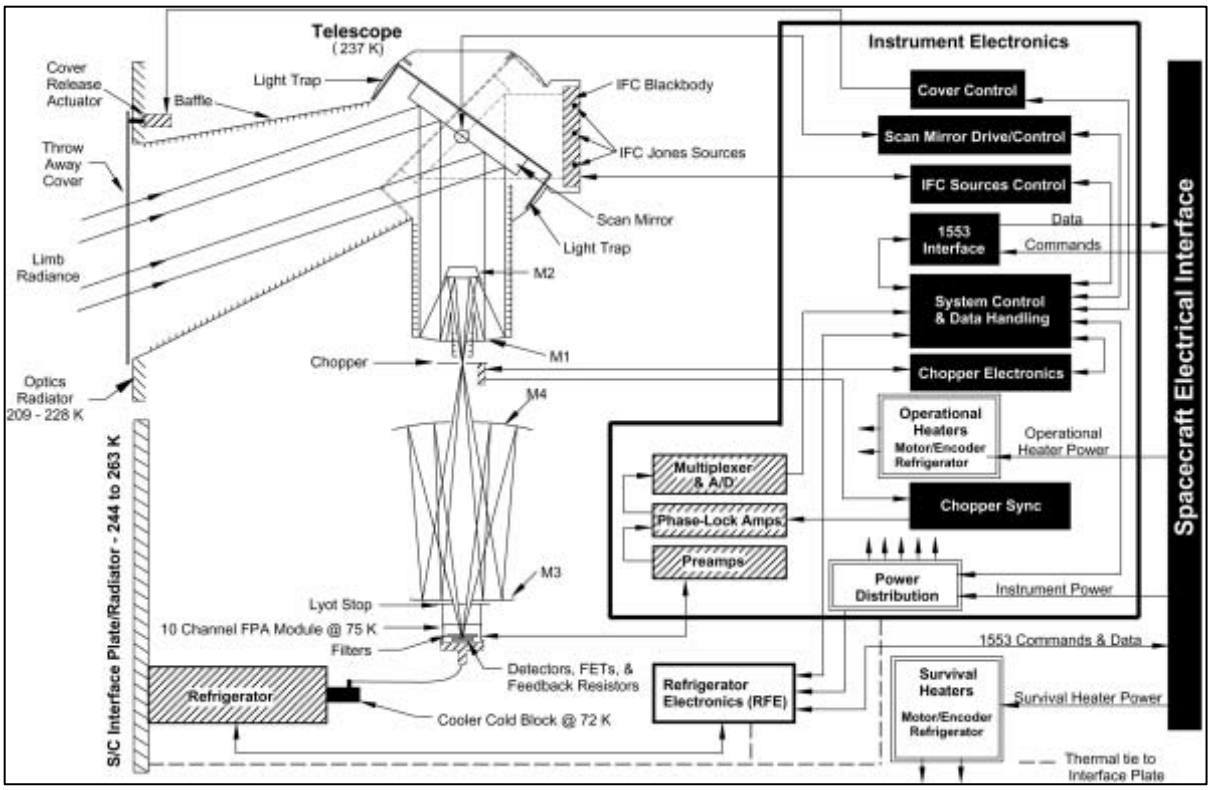

Figure 8. SABER instrument functional diagram.

4.3 In-flight Tracking of Short-Term Changes

The on-orbit operation of SABER includes periodic updates to the responsivity coefficient for each channel. This update is based on a space look to characterize the sensor offset ($O_{ch,i}$) and an IFC look to measure the sensor response to a known radiance. The updated responsivity coefficient can be calculated using

$$R_{ch} = \frac{r_{c,IFC}}{N_{IFC}} \tag{2}$$

where R_{ch} is the updated peak radiance responsivity, $r_{c,IFC}$ is the corrected IFC response, N_{IFC} is the IFC radiance, and *ch* is the channel number. The on-orbit scene radiance is estimated by substituting the updated peak radiance responsivity, as shown in equation (2), into equation (1). For this reason, it is important and necessary to calibrate these IFC sources during ground calibration. The IFC sources were calibrated by transferring calibration of ground-based blackbodies to the IFC sources using SABER as a transfer radiometer.

4.4 Long-Term Absolute Calibration Tracking

The SABER instrument has shown remarkable calibration stability. The most important calibration factor for analysis of trends is absolute response stability, which is monitored by tracking the radiance-per-count scale factor as a function of time. As discussed in section 4.1, this quantity is operationally monitored by alternately viewing space (cold point) and the instrument IFC (warm point). The most important stability considerations for the longwave channels are changes in IFC blackbody emissivity and drift in circuitry used to monitor the IFC temperature. The IFC temperature monitor was predicted to have very little drift over the original 2-year mission (<0.02K), which along with the very high blackbody emissivity (>.99), contributes to the remarkable calibration stability for these channels. The shorter wave channels, OH and O2(1D) channels, use Jones sources for calibration and have also shown remarkable stability. The total scale factor changes, linearly fit over the life of the mission, are shown in Figure 9 for all channels in terms of change relative to the beginning of the mission. Changes are below 1% over the 20+ years of the mission for all but the $CO2_D$ (4.3 μm) and OH_B channels which are close to 1% and the NO channel (2.6%).

These scale factors are continuously monitored in-flight as part of the calibration procedure and are accounted for in the data processing. So, while these factors are a measure of instrument stability, they do not indicate a temporal drift in the data products; rather they can be viewed as upper limits on potential calibration error. The scale factor is dependent on the Focal Plane Array temperature that is continuously monitored and accounted for in the calibration procedure. Possible channel spectral response drifts are also inferred from radiance changes in each channel during detector cool down and no statistically significant drift has been detected during the life of the mission.

In summary, the SABER instrument is stable, it is performing well within design expectations and is expected to do so for many more years. There is no evidence of changes in the instrument that would lead to erroneous trends in the analyzed data. All subsystems are performing as designed with no evidence of degradation beyond design limits.

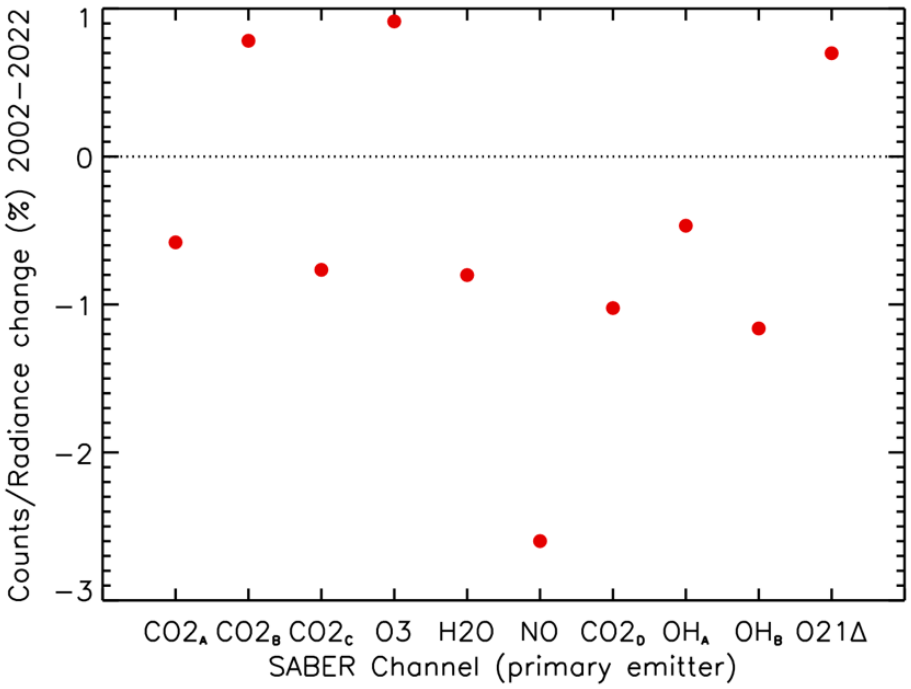

Figure 9. SABER total scale factor changes for each channel over 20+ years from January 2002 to July 2022, obtained by linear fits to daily values.

Electronic gain normalization was updated in 2009 after researchers noticed a scan mode difference in the SABER temperature and water products. Left panel of Figure 10 shows an example for temperature - note the horizontal features at roughly 55 to 60km and 40 to 45km. These features were traced to error in knowledge of the electronic gain step. That error can range from several tenths percent to several percent, depending on gain mode and channel. This was investigated 3 ways: 1- analyzing the entire SABER dataset for channels 1-7, 2- using a detailed examination of slow scan events taken on January 24, 2004, for channels 1-10, and 3- examination of a special scan sequence performed on October 30, 2009, that viewed the internal baffles and the IFC for channels 5-7. The first two analyzes were consistent for channels 1-4 and the latter two for channels 5-7, channels 8-10 were only analyzed using the slow scan. The final v2.0 gain steps shown in Table 9 were taken from the slow scan analysis. As seen in the right panel of Figure 10, use of these gain steps eliminates the horizontal features seen in the left panel. Note that even after the gain corrections are applied there are still residual differences between up and down scan modes. This may be due to detector relaxation effects for the up scan.

Table 9. On-orbit gain normalization.

Chan#	Medium Gain				Medium x Low				
	v1.07	Fit over dataset	Slow scan	V2.0	v1.07	Fit over dataset	Slow scan	Internal Scan	V2.0
1	1.0	1.0	1.0	1.0	21.114	20.731	20.65	*	20.65
2	7.8165	7.747	7.754	7.754	60.103	59.214	59.15	*	59.15
3	8.3178	8.255	8.260	8.260	68.857	67.816	67.90	*	67.90
4	13.454	13.320	13.333	13.333	183.56	179.80	180.09	*	180.09
5	12.547	12.427	12.459	12.459	152.92	147.09	150.33	149.63	150.33
6	19.157	19.040	18.965	18.965	209.57	201.78	206.43	205.71	206.43
7	8.6475	8.614	8.587	8.587	76.758	75.579	75.76	75.71	75.76
8	33.552	*	32.713	32.713	1108.44	*	1053.72	*	1053.72
9	32.730	*	31.912	31.912	1080.96	*	1031.81	*	1031.81
10	19.198	*	18.948	18.948	375.434	*	364.64	*	364.64

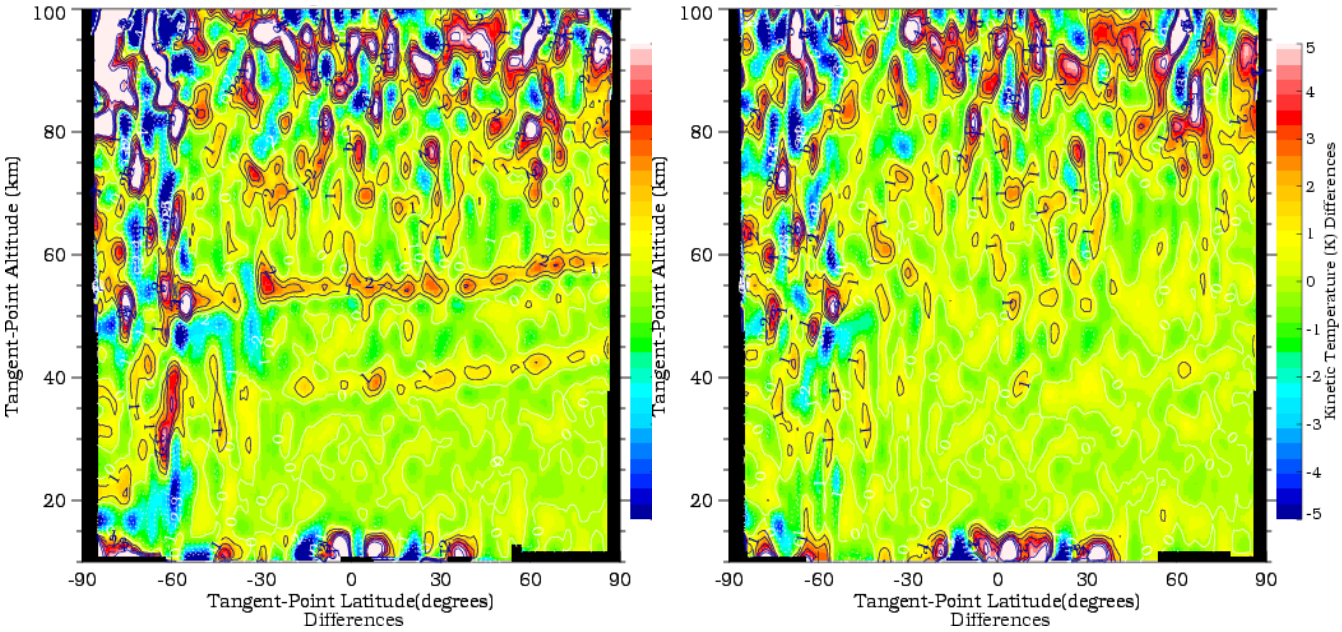

Figure 10. Up-down mode temperature difference for July 15, 2004, left panel v1.07 SABER, right v2.0.

Residual up-down differences in the long wave channels are very likely due to detector relaxation effects. Detector relaxation is a known problem for some of the channels during the up-scan measurement mode. It is caused by relaxation time of the detector to input signal. Scanning from high signal toward low signal can be a problem due to the scan rate being too fast for the detector to relax from the high signal input. This problem is particularly bad for the shortwave channels (8-10) and those channels have been corrected for this since the first data release. Prior to the v2.0 data analysis it had not been thought that the longer wave channels (1-7) were sufficiently impacted to warrant correction. However, while working to make water vapor an operational product, it was found to have an up-down mode difference that is very likely caused by detector relaxation. Temperature and ozone also appear to have significant, though relatively small up-down mode differences as well. This was corrected by applying a similar approach to that used for the shortwave channels. This approach involves determining coefficients, ***a*** and ***b***, for use in a signal correction, *C*, based on an exponential time decay function. That is, for each time, $t(i)$, determine a correction coefficient:

$$C(t(i)) = \boldsymbol{a}\sum N(t(j))\exp(\boldsymbol{b}(t(i)-t(j))) \qquad (3)$$

where *N* is signal and the summation is over j=0, i-1. Practical application requires analysis of a large set of up and down scans to derive the ***a*** and ***b*** coefficients and then applying the derived time decay function to each up-scan event. This procedure has been implemented and is operational in v2.0. Impact on retrieved temperature are shown in Figure 11, note that the spikes at about 45 and 60 km for the v1.07 data are due to errors in gain correction. The small (2 K) difference in the 80 – 90 km region is greatly reduced with the application of detector relaxation correction.

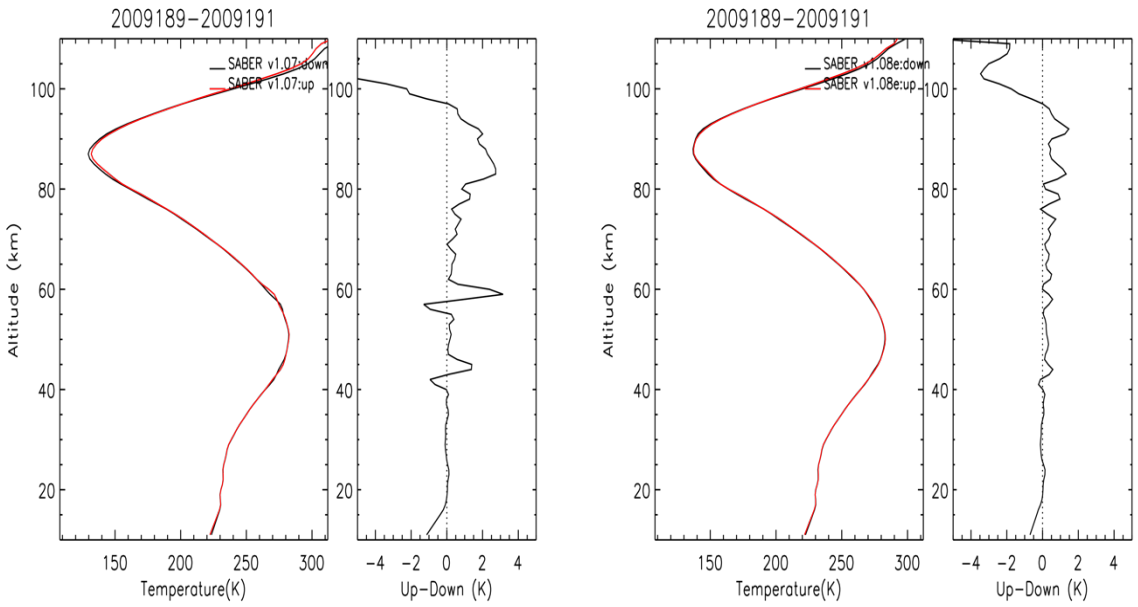

Figure 11. Average up – down node differences for July 8-10, 2009, left - v1.07, right - preliminary v2.0 with detector relaxation correction.

4.5 Validation

Recent work [1] comparing SABER mean stratosphere temperatures to those measured by the COSMIC Global Positioning System Radio Occultation (GPS- RO), indicate that SABER temperature is stable to within 0.1-0.2 K/decade or better depending on altitude. This is roughly commensurate with less than 0.1%/decade drift in radiometric calibration for the 15μm CO_2 channels. This is a remarkable achievement for a broadband radiometer.

5 SABER Measurement Algorithm Descriptions

5.1 Theoretical Basis and parameter descriptions

Several of the geophysical parameters in Table 2 require analysis that involves detailed radiative transfer (RT) modeling of the limb-path radiance observed by the instrument. Detailed RT models are required for retrieval of temperature and pressure (channels 1, 2, and 3), and volume mixing rations (VMR) for carbon dioxide (channel 7), ozone (channel 4), and water vapor (channel 5). Products derived from the other channels (channels 6, 8, 9, and 10) require retrieval of volume emission rates (VER) from the measured emission profiles. Section 5.1.1 describes the general RT and retrieval approaches used in these analyses, including extensions added to address NLTE.

5.1.1 Radiative transfer and retrieval techniques

The choice of RT and retrieval methods that can reasonably be used to analyze the SABER data is highly constrained by the size of the dataset and the complexity of the RT model. The retrieval of geophysical quantities such as temperature from limbpath scans is a highly non-linear problem and requires the iteration of a rigorous forward model comprised of detailed RT and instrument models. The raw data from SABER consists of over 1400 scans of the Earth limb per day for 10 channels with each scan sampling full path radiance for over 1000 limbpaths with tangent altitudes ranging from the ground to 400 km. Retrievals are typically limited to the 10 to 140 km range but this still requires multiple iteration of the forward model for nearly 350 limbpaths for each channel used to produce each product for each scan. This alone requires use of an approximate RT method rather than line-by-line. Even so, this is a difficult problem even for LTE and is greatly complicated when NLTE is considered. Since the populations of all energy states of a gas for a layer in LTE is dependent only on local temperature (the Boltzmann distribution) and consequently the source function is also a function of only temperature (the Planck function), the broadband radiance can be modeled with only a few separate emission species (gases). For NLTE every state must be modeled separately, and each iteration of the model must account for changes in the population distribution using a complex vibrational temperature model. For example, the NLTE forward model used in the temperature retrieval requires calculation of vibrational temperature for 41 separate bands and of limbpath radiance for 19 separate bands. Fortunately, retrieval of parameters from limbpath scans can be accomplished using the simple non-linear retrieval method known as the onion peel method, Russell and Drayson [118]. This is the approach taken for the SABER products that require iteration of complex RT models.

5.1.1.1 Broadband Radiative Transfer method

Analysis of some of the SABER data products requires accurate modeling of total band integrated limbpath radiance, *L*, for each measured sample. For LTE conditions this is defined as:

$$L = -\int_{\nu_1}^{\nu_2} f(\nu) \int_0^{\infty} B(\nu,s) \frac{\partial \tau(\kappa(\nu,s),u(s))}{\partial s} \partial s \partial \nu \qquad (4)$$

where:

s = distance from the instrument along the line of sight,

ν = wavenumber (cm^{-1}) with ν_1 and ν_2 spanning the non-zero region of $f(\nu)$,

f = the spectral band pass,

B = Planck function,

τ = transmission of the atmosphere along the line of sight,

κ = absorption coefficient along the line of sight,

u = absorber amount along the line of sight.

The SABER dataset is far too large for practical use of modern line-by-line algorithms to evaluate (4) in the operational inversion of the raw data. A fast and accurate radiative transfer (RT) model is required. BandPak [89] is used for the SABER analysis. Bandpak has been used as the RT model for several successful missions including HALOE [121], CLAES [114], and SOFIE [105]. It has also been used as the RT model for version 6 LIMS [113][101].

The calculations performed by BandPak are based on the emissivity growth approximation (EGA), [104]. For monochromatic applications this method provides a rigorous numerical representation of equation (4) by summing contributions to the total path radiance, L, of successive segments of the line of sight. The radiance through segment i is given by the relationship:

$$L_i = L_{i-1} + b_i[e_i(\kappa(\nu,s),u(s)) - e_{i-1}(\kappa(\nu,s),u(s))] \quad (5)$$

where:

i = path segment index,

b_i = the source function for segment i,

$e_i = 1 - \tau_1\tau_2\tau_3 \ldots \tau_i$, the composite emissivity through segment i, a function of κ and u.

Equation (5) simply states that the contribution of segment i to the total path radiance is a product of the source function evaluated at segment i and the emissivity growth resulting from the addition of segment i as viewed from the instrument. The EGA approximation is exact for monochromatic applications that are comprised of a sequence of homogeneous cells. It is extended to broadband applications by replacing b and e with broadband values determined from pre-calculated tables, [89]. The tables used with Bandpak for SABER are created using the line-by-line algorithm Linepak, [90] and the 2000 release of the HITRAN, [117], transition data. These tables include the band integrated Planck function (the source function for LTE) evaluated over a wide range of temperature and the band integrated emissivity evaluated over a wide range of temperature, pressures, and mass path. For NLTE applications the tables also include

band integrated Boltzmann factor (population ratio for LTE) tabulated over the same temperature range as the Planck function.

5.1.1.2 Extension to non-LTE

BandPak was originally written for LTE applications but was extended to non-LTE (NLTE) applications in 1998 in preparation for SABER data analysis. This extension is realized by the inclusion of factors used to adjust the LTE source function and optical mass similar to those described in Edwards et al. [96]. This approach was first demonstrated for the broadband EGA technique by Mlynczak et al. [88]. These factors account for the change from LTE in the state population distribution for the conditions being modeled. A consequence of the NLTE model is the requirement to separately model all significant vibrational bands and for Bandpak this requires pre-calculated source function and emissivity data for each band. For a given vibrational-rotational band it is assumed that the rotational states are in LTE so that only the vibrational state populations may be NLTE. This assumption greatly simplifies the problem and is sufficient for the transitions modeled for SABER.

The LTE population distribution is governed by thermal collisions and is represented by the Boltzmann distribution that, for any transition, represents the ratio of upper state to lower state populations by the Boltzmann factor,

$$\Gamma = \frac{g_1}{g_2}\frac{\bar{n}_2}{\bar{n}_1} = \exp(-hc\nu/kT_k), \qquad (6)$$

where:

h = Planck constant,

k = Boltzmann constant,

c = speed of light

ν = transition energy in wavenumber, cm^{-1},

T_k = kinetic temperature,

n_1 = population of lower state, overbar indicates LTE,

n_2 = population of upper state, overbar indicates LTE,

g_1 = lower state statistical weight (degeneracy),

g_2 = upper state statistical weight (degeneracy).

In equation (6) and all equations in this section, an overbar indicates a parameter pertains to LTE conditions. Deviation from the LTE condition is a consequence of non-thermal processes (e.g., spontaneous emission, radiative excitation, photolysis) significantly impacting the population distribution. By defining ratios of NLTE/LTE populations the upper to lower state population ratio for the general case can be stated as:

$$\frac{g_1}{g_2}\frac{n_2}{n_1} = \frac{r_2}{r_1}\Gamma \tag{7}$$

where:

$r_2 = n_2/\overline{n}_2$,

$r_1 = n_1/\overline{n}_1$.

From the definition of the monochromatic absorption coefficient, $\kappa(\nu)$, for the general case and for the LTE case, a NLTE/LTE ratio, $\alpha(\nu)$, of the monochromatic absorption coefficient can be defined, [96]:

$$\alpha(\nu) = \frac{\kappa(\nu)}{\overline{\kappa}(\nu)} = \frac{\overline{Q}_{Vib}}{Q_{Vib}} r_1 \left[\frac{1 - \frac{r_2}{r_1}\Gamma}{1 - \Gamma} \right] \tag{8}$$

where the LTE/NLTE ratio of Q_{Vib} accounts for the departure from LTE of the temperature correction to the vibrational partition function. By definition the NLTE/LTE ratio of $\tau(\nu)$ is also defined by $\alpha(\nu)$. And similarly, the NLTE/LTE ratio, $\beta(\nu)$, of the monochromatic source function is defined as:

$$\beta(\nu) = r_2/\alpha(\nu) \tag{9}$$

Thus equation (4) can be extended to NLTE:

$$L = -\int_{\nu_1}^{\nu_2} f(\nu) \int_0^{\infty} \beta(\nu) B(\nu,s) \frac{\partial \tau\left(\alpha(\nu,s)\kappa(\nu,s)u(s)\right)}{\partial s} \partial s \partial \nu \tag{10}$$

And the Bandpak equivalent is:

$$L_i = L_{i-1} + \beta_i b_i [e_i(\alpha_i(\nu,s)\kappa(\nu,s),u(s)) - e_{i-1}(\alpha_i(\nu,s)\kappa(\nu,s),u(s))] \quad (11)$$

where β_i and α_i are broadband correction factors. Recognizing that α and β are defined such that the only spectrally varying parameter is Γ, broadband values for β_i and α_i can be determined directly from r_1 and r_2 by using a broadband Γ. As discussed in Mlynczak et al. [88] for many applications it is sufficient to simply use the transition band center for determination of these correction factors. For more general use, Bandpak uses a line-strength weighted mean value of Γ that considers all transition lines over the band. This value is tabulated on the same temperature grid as the Planck function and α_i and β_i are determined by using equations (8) and (9) and the Γ corresponding to the temperature of cell i. The NLTE Bandpak RT errors are comparable to the LTE errors, with the NLTE Bandpak results typically within 1% of line-by-line results.

The factors r_1 and r_2 are determined from detailed modeling of all significant processes that impact the population of states important to the RT calculation of a specific SABER bandpass. The models used on the SABER project represent the population of state m by defining a vibrational temperature:

$$\mathrm{Tv_m} = \frac{E_m}{k \ln\left(\frac{n_0}{n_m}\frac{g_m}{g_0}\right)} \quad (12)$$

where E_m is the energy level of the state. The NLTE/LTE ratio for state m is then given by:

$$r_m = \exp\left[-\frac{E_m}{k}\left(\frac{1}{Tv_m} - \frac{1}{T_K}\right)\right] \quad (13)$$

The vibrational temperature models used in the analysis of SABER derived parameters are briefly discussed (if relevant), in sections 5.2.

5.1.1.3 Volume Emission Rates

Some SABER derived geophysical products (energetics products, atomic oxygen, atomic hydrogen, etc.) require the calculation of volume emission rates (VER). Equation (11) can be written:

$$\Delta L_i = J_i \Delta e_i \tag{14}$$

where: ΔL_i is the contribution to total path radiance for segment i, J_i is the source function of segment i, and Δe_i is the growth in total path emissivity contributed by segment i. For the optically thin limit where Δe_i equals the emissivity of segment i,

$$\mathrm{L} \simeq \frac{1}{4\pi} \sum_i V_i \Delta s_i \tag{15}$$

where V_i is the volume emission rate (VER) of the segment and Δs_i is the segment path length. For SABER analysis this is written as a matrix equation,

$$4\pi \boldsymbol{R} = \boldsymbol{A}\boldsymbol{V} \tag{16}$$

where $\boldsymbol{R}$ is a vector of SABER measured limbpath radiances, $\boldsymbol{A}$ is a matrix of known path segment lengths and $\boldsymbol{V}$ is a vector of unknown broadband VERs that is solved by inversion. The V_i determined by solving equation (16) are filtered by the SABER bandpasses. Total emission band values are determined by using the un-filtering method discussed in Mlynczak et al. [74].

The optically thin assumption provides adequate accuracy for the NO and OH VERs determined from SABER channels 6, 8, and 9. However, channel 10, which is used to determine ozone VMR from the 1.27 μm dayglow, begins to depart from the optically thin case at about 75 km and we wish to determine ozone VMR from this channel to at least 60km. This requires a more rigorous treatment, [45], which uses Bandpak to perform an onion peel retrieval of J_i, and then calculates the volume emission rates as:

$$V_i = 4\pi J_i \frac{d\varepsilon}{ds} \tag{17}$$

where $\frac{d\varepsilon}{ds}$ is the emissivity gradient at the tangent point, determined from the Bandpak emissivity tables.

5.2 Conversion of SABER Instrument Signals to Geophysical Parameters

5.2.1 Measurement Equations

Retrieval of geophysical parameters from measurements of limbpath emission typically requires the iteration of a forward model and varying one or more forward model variables until modeled emission matches measured to within measurement precision. There are many ways this can be done but as discussed in section 5.1.1 we use the onion peel method for retrievals that require such iteration. The onion peel retrieval is equivalent to inversion of a diagonal matrix, only requiring sensitivity of the forward model to tangent layer changes. For a linear system, as discussed in [116], the retrieval for each tangent point can be written as:

$$x_i = \frac{y_i - \sum_{j=i+1}^{n} K_{ij} x_j}{K_{ii}} \tag{18}$$

where x_i is the atmospheric parameter we wish to retrieve at tangent point i, y_i is the measured emission for the limbpath tangent at i, and K_{ij} is the sensitivity of the forward model at level i to x_j. In practice the retrievals are typically nonlinear requiring iteration of each tangent altitude, with the retrieval proceeding sequentially from the highest tangent altitude to the lowest.

5.2.1.1 Kinetic temperature and pressure

The retrieval of kinetic temperature, T, and atmospheric pressure is achieved for LTE conditions using a method similar to that developed by Gille and House [99]. This method uses 2 CO_2 channels in the 15 μm region, a wide channel and a narrow channel. The method starts by assuming a pressure (P_0) at a reference altitude (z_0). For a given P_0, T and pressure, P, are retrieved at and above z_0 for each channel by matching a simulated radiance profile to the measured radiance profile with hydrostatic equilibrium constraining the solution. This procedure requires knowledge of the mixing ratio profile of CO_2, which for the SABER algorithm is taken from the Whole Atmosphere Community Climate Model (WACCM), [98]. The key observation made by Gille and House is that a hydrostatically constrained single channel retrieval will return the correct temperature at the tangent point where optical depth to the tangent point is equal to unity, regardless of error in assumed P_0. Thus, a second channel with unit optical depth at a significantly different pressure will uniquely define a $T(P)$ profile (for no measurement noise and perfect radiance simulation model). To reduce retrieval error due to measurement noise and forward model error,

the SABER algorithm iterates P_0 until $T(P)$ retrieved from one channel best matches that retrieved from the other over a limited altitude (or pressure) range. For SABER, the $T(P)$ matching between channels is performed over a pressure range of approximately 3-15 mb. After P_0 is set, T and P are retrieved for all limbpath tangent points by matching radiance measured in one of the bands and constraining the solution using hydrostatic equilibrium.

The LTE assumption used in finding P_0 is invalid at higher altitudes, and T and P retrieval requires iteration of the NLTE RT model discussed in section 5.1.1.2. The *Tv* required for this are determined using a technique similar to that developed by Curtis, [95], to calculate radiative heating rates. The SABER algorithm employs a Modified Curtis Matrix formulation [107, 108] and uses BandPak for the RT calculations required to fill the matrix, [31, 26]. This model considers all processes that significantly impact the populations of energy states required to accurately model the SABER 15 and 4.3 μm CO_2 channels. The vibrational temperatures produced by the SABER CO_2 model have been validated against those produced by several independent models, [106], [107], [108] with differences typically within 1 K for the most significant energy levels when using the same reaction rates. Model error in the upper mesosphere and lower thermosphere (LTE is valid below 60 km) is dominated by uncertainty in the reaction rates and population of the reacting partners (e.g., atomic oxygen) rather than insufficiency of the model itself, [31] [17].

5.2.1.2 Carbon dioxide

Carbon dioxide is retrieved from 65-125 km for daytime measurements as part of a post-processing that retrieves both temperature and CO_2 VMR using 2 channels, one in the 15 μm region (channel 1) and one in the 4.3 μm region (channel 7). This procedure uses an independent RT model and is described by Rezac et al [11].

5.2.1.3 Ozone (9.6 μm)

Ozone VMR is retrieved using a channel in the 9.6 μm region (channel 4). Analysis of ozone infrared emission measurements from LIMS [122] showed that the high-lying ν_3 hot bands are chemically pumped and that uncertainty in the production and loss rates of these high-lying states may result in large uncertainty in the retrieved ozone concentration. For this reason, the SABER ozone spectral bandpass was chosen to effectively eliminate the contribution from most ozone hot-bands longward of 1010 cm^{-1} while maintaining most of the contribution from the strong ν_3 fundamental as well as most of the much weaker ν_1 fundamental band, providing good measurement sensitivity from the lower thermosphere to the middle

stratosphere. Similar to the retrieval of T(P), this requires iteration of a NLTE RT model at higher altitudes. The algorithm used for calculating the requisite vibrational temperatures is based on the method described by Mlynczak and Drayson [41] [42] [43], who showed that the only radiative process that need be considered is absorption of upwelling radiation. This allows a much simpler model than that used for CO_2. The ozone NLTE model, in addition to the radiative absorption, requires modeling only local photochemical and quenching processes. This method defines a system of statistical equilibrium equations that are expressed in matrix form and solved directly by matrix inversion. Though this method is simpler than the Curtis matrix method used for CO_2, excited O_3 is produced mostly by photochemical reactions and the steady state energy distribution of these molecules depend on the photochemical balance assumptions used in the model.

The ozone spectral bandpass also includes emissions from the laser bands of CO_2. These emissions are modeled using the NLTE model discussed in section 5.1.1.2 and 5.2.1.1 and are accounted for in the retrieval of ozone VMR.

5.2.1.4 Ozone (daytime, 1.27 μm)

Ozone is retrieved for daytime data using observations from the 1.27 μm channel (channel 10). This retrieval uses the 1.27 μm VERs (see section 5.1.1.3) along with a non-LTE radiative and kinetic model to derive profiles of ozone VMR [45], [49], [51]. This retrieval is similar to that used to retrieve ozone from the Solar Mesosphere Explorer, which was launched in 1981 [125]. Figure 12 shows a schematic diagram of the path of energy from the absorption of solar radiation by ozone or O_2 to the emission of a 1.27 μm photon. The retrieval process thus needs to account for all the losses of energy, including quenching and spontaneous emissions [51].

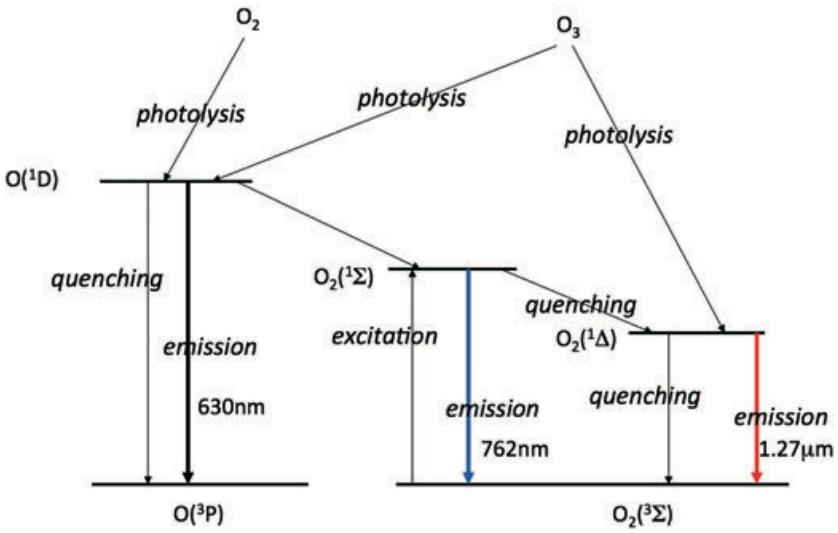

Figure 12. Schematic diagram of energy paths from the photolysis of O_2 or O_3 in the mesosphere. The red arrow indicates the 1.27 μm emission used to retrieve SABER daytime ozone. Adapted from Mlynczak et al. [51].

5.2.1.5 Water vapor

Water vapor VMR is retrieved from a channel in the 1.6 μm region (channel 5). This retrieval also requires iteration of a NLTE RT model. The vibrational temperature algorithm used for SABER H_2O is based on a Curtis matrix approach similar to that used for CO_2. The processes and rates included in the SABER algorithm are based on those discussed in references [55] and [109]. The SABER vibrational temperature algorithm compares well to other algorithms [97]. The SABER H_2O channel (channel 5) is suspected to include significant out-of-band (OOB) contributions from the vicinity the 9.6 μm ozone band. The OOB mechanism was estimated from a detailed comparison to MLS by fitting modeled SABER radiance including possible OOB contributions to provide a best fit of SABER retrieved H_2O to MLS H_2O. This analysis resulted in a correction to the H_2O channel radiance using the SABER measured ozone channel radiance and the first public release of SABER H_2O with the version 2.07 release [53].

5.2.1.6 Atomic oxygen

Atomic Oxygen, O, is derived both day and night from photochemical models and SABER measurements ozone and, for nighttime, SABER measurements of OH VER. During the daytime ozone abundance is assumed to be in photochemical steady state, i.e., the production of ozone by recombination is balanced by photolysis in the Hartley band, equation (19). O is derived from this equation and SABER retrieved ozone [45][65].

$$k_2[O][O_2][M] = J[O_3] \quad (19)$$

In equation (19), k2 is the recombination rate coefficient, [O], [O_2], [O_3], and [M] are the concentrations of atomic oxygen, molecular oxygen, ozone, and the total number density, and J is the photolysis rate (/s) of the Hartley band. The total number density is from SABER retrieved T(P), ozone number density is derived from the 9.6 μm SABER retrieval, O_2 number density is derived using 0.21 VMR.

The retrieval of O for nighttime is also based on photochemical balance. For this case, the production of ozone by recombination is balanced by loss of ozone through reaction with atomic hydrogen, H [60][65].

$$k_4[H][O_3] = k_2[O][O_2][M] \quad (20)$$

In equation (20), k4 is the rate coefficient for the reaction of H and O3 which produces vibrationally excited OH in the υ=9, 8, 7, and 6 states. Because SABER channel 8 observes the 9–7 and 8–6 emission in the 2.0 μm region, it is only necessary to construct a model of the emission from the υ = 9 and υ = 8 states. The OH emission intensity observed by SABER is directly proportional to the product k4[H][O3], and thus, the emission intensity is directly proportional to the O-atom concentration via equation (20). The proportionality factor needed to complete the retrieval is derived from the relatively simple channel 8 emission model described in [65].

5.2.1.7 Atomic hydrogen

Since the left-hand side of equation (20) is directly proportional to the OH emission measured by SABER channel 8, atomic hydrogen is retrieved from SABER channel 8 radiance, the proportionality factor derived from the channel 8 emission model, and SABER retrieved ozone [60][65][67].

5.2.1.8 Energetics parameters

One of the main goals of SABER is to determine the energy budget of the mesosphere and lower thermosphere (MLT). SABER measured emissions are used along with photochemical models to estimation of over 30 energy budget terms related to heating (both solar and chemical) and cooling

(through emission) of the atmosphere [91]. Details of these calculations are given in the referenced papers and will not be presented here.

SABER provides global measurements of critical infrared emissions from CO_2 (15 μm), O_3 (9.6 μm), NO (5.3 μm), OH (1.6 μm; 2.0 μm), O_2 (1.27 μm,) and CO_2 (4.3 μm). Emissions from 15μm CO_2 and 5.3 μm NO dominate the infrared radiative cooling of the Earth's upper atmosphere [68][72][73][74][75], and SABER measurements of these emissions have been used to create a Thermospheric Climate Index (TCI) [69]. Emissions from 9.6 μm ozone emissions are important to the radiative energy balance in the mesosphere and emissions from oxygen and hydrogen (e.g., $O_2(1\Delta)$ and OH [77]) are significant in the upper mesosphere. OH emissions in the Meinel bands are also important in the energy budget because a significant amount of the chemical potential energy released during the reaction of H and O_3 may be radiated by the product OH molecule resulting in chemiluminescent loss [70][78]. SABER measurements of these OH band emissions are used to estimate these losses.

5.3 Signal Estimates and Error Analysis

As discussed in section 5.2.1, the onion peel retrieval is equivalent to inversion of a diagonal matrix. However, the errors involve off-diagonal terms since error in non-tangent layers also impact results. Our technique calculates an error variance associated with the sensitivity of the forward model to a change in the tangent layer only, and that can be far from sufficient as the optical depth of the limb paths increases. For some SABER parameters we perform Monte-Carlo studies of major errors for several atmospheres and report those results as an estimate of expected errors. This approach allows looking at model errors, and other instrument errors one wouldn't typically include in an operational analysis. For parameters that use linear retrievals, errors are estimated directly from the models used in the retrieval.

5.3.1 Temperature

Table 10 gives estimates of precision (random error) and systematic error for SABER retrieved kinetic temperature, T_k, at specified altitudes for a typical mid-latitude atmosphere. These errors are representative of most cases (both day and night), however, for polar summer mesopause events, systematic errors above 80 km are expected to be higher due to higher uncertainty in the vibrational temperatures calculated for these very cold conditions. The values in this table are a compilation of error estimates from various Monte-Carlo studies including those discussed in [16] and [17]. These errors include errors in interfering species, spectroscopy, rate coefficients (for NLTE models), and other inputs.

Table 10. Estimated errors for SABER temperature.

Altitude (km)	15	20	30	40	50	60	70	80	85	90	95	100	105	110
Precision (K)	0.3	0.3	0.3	0.6	0.6	0.7	1.0	1.8	2.2	3.6	5.4	6.7	9.0	15
Systematic Error (K)	1.4	1.2	0.7	1.5	1.9	1.9	1.5	1.4	3.1	4.0	3.7	5.0	11	25
RSS of Random & Systematic Errors (K)	1.4	1.3	0.8	1.6	2.0	2.1	1.8	2.3	3.8	5.4	6.5	8.4	14	29

5.3.2 Carbon Dioxide

Carbon dioxide is retrieved for daytime data (SZA<80º) as part of a post-process that uses 2 channels, one at 15 µm and one at 4.3 µm [11] to retrieve both T_k and CO_2 VMR. Table 11 summarizes the CO_2 errors estimated from Monte-Carlo analysis.

Table 11. Estimated error for 2 channel retrieval of CO_2.

2-Channel CO_2 Retrieval	**70 km**	**80 km**	**90 km**	**100 km**	**110 km**	**125 km***
CO_2 VMR prec. (%)	1	1	1	1	2	2
CO_2 VMR systematic (%)	15	15	12	21	32	22
RSS Syst. & Prec. CO_2VMR (%)	15	15	12	21	32	22

* CO_2 VMR above 110 km is based on WACCM T, O, O(^{1}D). The error at 125 km will become smaller as the non-LTE influence of O(^{1}D) on the CO_2 populations becomes weaker.

5.3.3 Ozone (9.6 µm)

Table 12 gives results of detailed Monte-Carlo analysis for ozone retrieved from the SABER 9.6µm channel for some pressures levels (roughly equivalent to altitudes from 15 km to 70 km). These error estimates are valid for most cases (both day and night). The error analysis and validation against other measurements are described in [35]. Comparisons [32] to other satellite measurements indicate that SABER derived from the 9.6 µm channel likely has a positive bias in the mesosphere below about 85km.

Table 12. Estimated Errors for 9.6 µm SABER Ozone.

Error type	Pressure-altitude (hPa)						
	100	50	10	3	1	0.4	0.1
Random Errors							
Measurement noise	0.5	0.3	0.2	0.1	0.2	0.4	1.0
Jitter (20 meters)	8	6	2	1	1	0.8	0.5
1. Total Precision[a]	8	6	2	1	1	1	1
Systematic Errors							
Calibration (1%)	3	4	5	3	2	2	2
Line Intensity (4%)	4	4	4	4	4	4	4
Line Halfwidth (10%)	2	2	3	3	2	2	2
Band Model[b]	8	5	3	2	1	0.5	0.5
T(P) error[c]	20	15	7	5	7	7	7
2. Total Systematic Error	22	17	10	8	9	9	9
Total Estimated Errors RSS of 1 and 2, nearest %	23	18	10	8	9	9	9

a- Total Random Error calculated as RSS of individual random error sources - these errors are reduced by the interleave average procedure.
b- Band model errors from comparison to line-by-line for Standard atmosphere.
c- T(P) error is based on validation results discussed in Remsberg et. al. [16].

5.3.4 Ozone (1.27 µm)

Ozone is retrieved for daytime (SZA<80º) using emissions measured from the SABER 1.27 µm channel in conjunction with a photochemical model [45]. Generally good results are achieved except for the times around sunrise and sunset at which times ozone can be overestimated by up to a factor of 2. Though we have not performed detailed error analysis for this product, comparisons to other satellite instruments, as discussed in [32], suggest better results can be obtained for this product in the 60-85 km altitude region than for the 9.6 µm channel for daytime data well after sunrise and well before sunset.

5.3.5 Water vapor

Table 13 gives a summary of errors estimated from detailed Monte-Carlo studies for water vapor. These estimates are valid for most cases (both day and night). The error analysis and comparisons of this product to other instruments are described in [53].

Table 13. Estimated Errors for SABER H_2O.

	Trop	20 km	30 km	40 km	50 km	60 km	70 km	80 km[e]
Random Error Sources								
Measurement Noise	1.00	1.00	1.00	1.00	1.50	3.00	10.00	30.00
Jitter(20m)	3.00	2.50	2.00	1.50	1.50	1.50	1.50	1.50
Total Random Error[a]	3.16	2.69	2.24	1.80	2.12	3.35	10.11	30.04
Systematic Error Sources								
Non-LTE Model	0.00	0.00	0.00	0.50	1.00	3.00	7.00	15.00
Spectroscopy	1.00	1.00	1.00	1.00	1.00	1.00	1.00	1.00
Interfering Gases	2.00	2.00	2.00	1.50	1.00	0.50	0.50	0.50
Temperature[b]	20.00	15.00	12.00	10.00	10.00	12.00	12.00	12.00
Radiance Calibration (1%)	5.00	3.00	2.50	2.00	2.50	3.00	2.50	2.00
Registration(50m)	3.00	2.50	2.00	1.00	2.00	3.00	3.00	3.00
Total Systematic Error[c]	20.95	15.66	12.62	10.42	10.64	13.12	14.47	19.58
Total Estimated Error[d]	21.19	15.89	12.82	10.57	10.85	13.55	17.66	35.85

a- Total Random Error calculated as RSS of individual random error sources - these errors are reduced by the interleave average procedure.
b- Temperature error based on validation results discussed in Remsburg et al. [16].
c- Total Systematic Error calculated as RSS of individual systematic sources.
d- Total Estimated Error is RSS of systematic and random errors and is an upper bound.
e- 80 km estimates are valid for daytime only. Nighttime data at 80 km has very low signal to noise and results are predominately from a-priori climatology.

5.3.6 Atomic oxygen

No detailed error analysis has been performed for atomic oxygen. However, SABER atomic oxygen results are discussed in [59] [60] [63] [64] and [65].

5.3.7 Atomic hydrogen

No detailed error analysis has been performed for atomic hydrogen. However, SABER atomic hydrogen results are discussed in [66] and [67].

5.3.8 Energetics parameters

No detailed error analysis has been performed for the energetics parameters. However, SABER energetics results are discussed in [68] [69] [70] [71] [72] [73] [74] [75] and [76].

5.4 Preflight Calibration Algorithms

As discussed in section 4.2, the preflight calibration of SABER involves the characterization of response as a function of channel as described by equation (1). The parameters of that equation must be fully characterized for all anticipated instrument environments and measurement modes. This characterization is primarily accomplished preflight in the laboratory and transferred to the on-orbit environment as discussed in section 4.3, though, as discussed in section 4.4, some of these characterizations are monitored and corrected using on-orbit measurements. The preflight calibrations used to characterize equation (1) require numerous complex algorithms that we will not review with this document since they are fully detailed in the SDL ground calibration report, SDL/99-155, and summarized in Tansock et al. [3].

Appendix A: List of SABER variable definitions

Table A.1 describes the contents of the SABER L1B NetCDF files. This table lists each variable contained in the netCDF file along with its type, dimensions, units, long name, and missing value. The L1B dimensioning variables are: Channel= 10, elevation:1401, pressure_nmc:64, vector: 3, str_len:6, event: UNLIMITED. The event dimension will depend on the number of events in the netCDF file. Note that 3 public versions of the Level1B files have been processed: version 1.04 (used for processing version 1.06 L2), 1.07 and 2.0.

Table A.1. Level 1B variables.

variable(dimensions)/type*	Units	Long name	Missing value	Version**
ChannelName(channel,str_len)/c				04 07 20
sigma(channel)/f				04 07 20
event(event)/s		Event Number for Current File	-9	04 07 20
preEvent(event)/s		Previous event indicator	-9	04 07 20
date(event)/i		Date [yyyyddd]	2001100	04 07 20
mode(event)/s		Mode (0=Down 1=Up)	-9	04 07 20
tpDN(event)/s		Tangent Point Day/Night (0=Day 1=Night,2=terminator (85<solar zenith angle<95))	-9	04 07 20
tpAD(event)/s		Tangent Point Asc/Des (0=Ascending 1=Descending)	-9	04 07 20
offsetALT(event)/f	km	Altitude offset from Level2	0	04 07 20
twistAngle(event)/f	degrees	Residual Twist Angle	0	04 07 20
motionFactor(event)/f		Residual Motion Scale Factor	1	04 07 20
moonSepAngle(event)/f	degrees	Separation Angle (los & moon)	-999	04 07 20
tpaltmoonSepAngle(event)/f	km	Tp Altitude at Separation Angle	-999	04 07 20
solAP(event)/f		Solar Ap Index	-9	04 07 20
solKP(event)/f		Solar Kp Index	-9	04 07 20
solf10p7Daily(event)/f		F10.7 Flux (Daily	-999	04 07 20
solF10p781dAvg(event)/f		F10.7 Flux (81-day Average)	-999	04 07 20
solSpotNo(event)/s		Zurich Sunspot Number	-9	04 07 20

scSolarZen(event)/f	degrees	Sc solar zenith angle	-999	04 07 20
earth_sun(event)/f	km	Earth-Sun distance	-999	04 07 20
lunar_vector(event,elevation,vecto r)/f		Vector to center of moon from spacecraft	-999	04 07 20
pressure_nmc(event,pressure_nmc)/f	mbar	NMC pressure at TP	-999	04 07 20
temperature_nmc(event,pressure_n mc)/f	K	NMC temperature at TP	-999	04 07 20
geopotential_height_nmc(event,pr essure_nmc)/f	km	NMC Geopotential Height		04 07 20
time(event,elevation)/i	msec	Time since midnight (UT)	-999	04 07 20
sclatitude(event, elevation)/f	degrees(N)	Spacecraft latitude	-999	04 07 20
sclongitude(event, elevation)/f	degrees(E)	Spacecraft longitude	-999	04 07 20
scaltitude(event, elevation)/f	km	Spacecraft altitude	-999	04 07 20
tplatitude(event, elevation)/f	degrees	Tangent point latitude	-999	04 07 20
tplongitude(event, elevation)/f	degrees	Tangent point longitude	-999	04 07 20
tpaltitude(event, elevation)/f	km	Tangent point altitude		04 07 20
tpSolarZen(event, elevation)/f	degrees	Tangent point Solar Zenith Angle	-999	04 07 20
tpSolarLT(event, elevation)/f	msec	Tangent point local solar time***	-999	04 07 20
elevation(event, elevation)/d	milliradian	Elevation Angle	-9999	04 07 20
scanAng(event, elevation)/d	milliradian	Mirror Scan Angle	-999	04 07 20
Rad(event, elevation, channel)/f	Watts/m2/sr	Calibrated Radiance	-999	04 07 20
scattitude(event, elevation, vector)/f	degrees	Spacecraft attitude vector	-999	04 07 20
maxRate(event)/f	degrees/sec	Maximum scan rate		04 07 20
timeMaxRate(event)/i	msec	Time corresponds to maximum scan rate		04 07 20
angleMaxRate(event)/f	degrees	Angle corresponds to maximum scan rate		04 07 20
qaRelaxationCorr(event, channel, vector)/f		QA for Relaxation Correction in Corrected Radiance	-999	04 07 20

qaRelaxationPctg(event, channel, vector)/f		QA for Relaxation Correction in Percent Total Radiance	-999	04 07 20
qaScatterCorr(event, channel, vector)/f		QA for Scatter Correction in Corrected Radiance	-999	04 07 20
qaScatterPctg(event, channel, vector)/f		QA for Scatter Correction in Percent Total Radiance	-999	04 07 20
tplatdeltaA(event, elevation)/f	degrees	Tangent Point Latitude Gradient Near Side	-999	20
tplondeltaA(event, elevation)/f	degrees	Tangent Point Longitude Gradient Near Side	-999	20
tplatdeltaB(event, elevation)/f	degrees	Tangent Point Latitude Gradient Far Side	-999	20
tplondeltaB(event, elevation)/f	degrees	Tangent Point Longitude Gradient Far Side	-999	20
perGreatArc(event)/f	degrees	Tangent Point Gradient Great Arc Change	-999	20

* f=float, d=double, s=short, i=int, c=char
** 04=1.04, 07=1.07, 20=2.0, RED means data unfilled for that version.
*** Description in Level1B files stating UT for this variable is incorrect

Table A.2 describes the contents of the SABER L2A files. This table lists each variable contained in the netCDF file along with its type, dimensions, units, long name, and missing value. The variables that are dimensioned use the variables: Altitude = 400, Event = UNLIMITED, and Vector =3. The Event dimension will depend on the number of events in the netCDF file. Vector is used only for a lunar vector variable. The variables that have the _top in the name are for the top half of the altitude range (extending to about 285km). The same variable without the _top extension is for the bottom half of the altitude range (roughly 15km to 155km). Note that there are several versions of Level2A data, the column to the far right indicates for which versions (starting with 1.06) a particular variable is included.

Table A.2. Level 2A variables.

Variable(dimensions)/type*	units	Long name	Miss. value	Version**
event(event)/s		Event Number for Current File		06 07 20

date(event)/i	yyyyddd	Date [yyyyddd]	-999	06 07 20
mode(event)/s		0=Down 1=Up	-999	06 07 20
tpDN(event)/s		0=Day 1=Night 2=Twilight	-999	06 07 20
tpAD(event)/s		0=Ascending 1=Descending	-999	06 07 20
moonSepAngle(event)/f	degrees	Angle between moon and LOS	-999	06 07 20
tpaltmoonSepAngle(event)/f	km	Tpaltitude used for moonSepAngle	-999	06 07 20
solAP(event)/f		Solar Ap Index	-999	06 07 20
solKP(event)/f		Solar Kp Index	-999	06 07 20
solf10p7Daily(event)/f	10^{-22} W/m2/Hz	F10.7 Flux (Daily	-999	06 07 20
***solF10p781dAvg(event)/f	10^{-22} W/m2/Hz	F10.7 Flux (81-day Average)	-999	06 07 20
solSpotNo(event)/s		Zurich Sunspot Number	-999	06 07 20
scSolarZen(event)/f	degrees	Sc Solar-Zenith Angle	-999	06 07 20
earth_sun(event)/f	km	Earth-Sun Distance	-999	06 07 20
L1_altoff(event)/f	km	Altitude Offset from Level1	-999	-- -- 20
Iaurora(event)/s		Aurora Flag (1=TRUE, 0=FALSE)	-999	06 07 20
time(event,altitude)/i	msec	Msec Since Midnight	-999	06 07 20
sclatitude(event, altitude)/f	degrees	Spacecraft Latitude	-999	06 07 20
sclongitude(event, altitude)/f	degrees	Spacecraft Longitude	-999	06 07 20
scaltitude(event, altitude)/f	km	Spacecraft Altitude	-999	06 07 20
tpaltitude(event, altitude)/f	km	Tangent-Point Altitude	-999	06 07 20
tplatitude(event, altitude)/f	degrees	Tangent-Point Latitude	-999	06 07 20
tplongitude(event, altitude)/f	degrees	Tangent-Point Longitude	-999	06 07 20
tpSolarZen(event, altitude)/f	degrees	Tangent-Point Solar-Zenith Angle	-999	06 07 20
tpSolarLT(event, altitude)/f	msec	Tangent-Point Local-Solar Time	-999	06 07 20
elevation(event, altitude)/d	milliradians	Elevation Angle	-999	06 07 20
time_top/i	msec	Msec Since Midnight	-999	06 07 20
sclatitude_top(event,altitude)/f	degrees	Spacecraft Latitude	-999	06 07 20
sclongitude_top(event, altitude)/f	degrees	Spacecraft Longitude	-999	06 07 20
scaltitude_top(event,altitude)/f	km	Spacecraft Altitude	-999	06 07 20
tpaltitude_top(event,altitude)/f	km	Tangent-Point Altitude	-999	06 07 20

tplatitude_top(event,altitude)/f	degrees	Tangent-Point Latitude	-999	06 07 20
tplongitude_top(event,altitude)/f	degrees	Tangent-Point Longitude	-999	06 07 20
tpSolarZen_top(event,altitude)/f	degrees	Tangent-Point Solar-Zenith Angle"	-999	06 07 20
tpSolarLT_top(event,altitude)/f	msec	Tangent-Point Local-Solar Time	-999	06 07 20
elevation_top(event, altitude)/d	milliradians	Elevation Angle	-999	06 07 20
tpgpaltitude(event, altitude)/f	km	Tangent-Point Geopotential Altitude	-999	-- 07 20
pressure(event, altitude)/f	mbar	Pressure	-999	06 07 20
Pressure_error(event, altitude)/f	mbar	Pressure Error	-999	06 07 --
ktemp(event, altitude)/f	K	Kinetic Temperature (merge)	-999	06 07 20
ktemp_error(event, altitude)/f	K	Kinetic Temperature Error	-999	06 07 --
density(event, altitude)/f	$1/cm^3$	Atmospheric Density	-999	06 07 20
density_error(event, altitude)/f	$1/cm^3$	Atmospheric Density Error	-999	06 07 --
O3_96(event, altitude)/f	Mixing ratio	O3 Mixing Ratio 9.6µm	-999	06 07 20
O3_96_error(event, altitude)/f		O3 9.6µm channel Error	-999	06 07 --
O3_127(event, altitude)/f	Mixing ratio	O3 Mixing Ratio 1.27µm Channel	-999	06 07 20
O3_127_error(event, altitude)/f		O3 1.27µm channel Error	-999	06 07 --
H2O(event, altitude)/f	Mixing ratio	H2O Mixing Ratio	-999	06 07 20
H2O_error(event, altitude)/f		H2O Error	-999	06 07 --
CO2(event, altitude)/f	Mixing ratio	CO2 Mixing Ratio	-999	06 07 20
CO2_error(event, altitude)/f		CO2 Error	-999	06 07 --
O2_1sigma(event, altitude)/f	Mixing ratio	O2(1sigma) Mixing Ratio	-999	06 07 20
O(event, altitude)/f	Mixing ratio	O Mixing Ratio	-999	06 07 20
H(event, altitude)/f	Mixing ratio	H Mixing Ratio	-999	06 07 20
O2_1delta_ver(event, altitude)/f	$ergs/cm^3/sec$	O2(1delta) VER	-999	06 07 20
O2_1delta_ver_error(event, altitude)/f	$ergs/cm^3/sec$	O2(1delta) VER Error	-999	06 07 --

OH_16_ver(event, altitude)/f	ergs/cm^3/sec	OH VER for 1.6 µm Channel	-999	06 07 20
OH_16_ver_error(event, altitude)/f	ergs/cm^3/sec	OH VER Error	-999	06 07 --
OH_20_ver(event, altitude)/f	ergs/cm^3/sec	OH VER for 2.0 µm Channel	-999	06 07 20
OH_20_ver_error(event, altitude)/f	ergs/cm^3/sec	OH VER Error	-999	06 07 --
NO_ver(event, altitude)/f	ergs/cm^3/sec	NO VER	-999	06 07 20
NO_ver_top(event, altitude)/f	ergs/cm^3/sec	NO VER	-999	06 07 20
NO_ver_error(event, altitude)/f	ergs/cm^3/sec	NO VER Error	-999	06 07 --
NO_ver_top_error(event, altitude)/f	ergs/cm^3/sec	NO VER Error	-999	06 07 --
O2_1delta_ver_unfilt(event, altitude)/f	ergs/cm^3/sec	O2(1delta) VER	-999	06 07 20
O2_1delta_ver_unfilt_error(event, altitude)/f	ergs/cm^3/sec	O2(1delta) VER Error	-999	06 07 --
OH_16_ver_unfilt(event, altitude)/f	ergs/cm^3/sec	OH VER for 1.6 µm Channel	-999	06 07 20
OH_16_ver_unfilt_error(event, altitude)/f	ergs/cm^3/sec	OH VER Error	-999	06 07 --
OH_20_ver_unfilt(event, altitude)/f	ergs/cm^3/sec	OH VER for 2.0 µm Channel	-999	06 07 20
OH_20_ver_unfilt_error(event, altitude)/f	ergs/cm^3/sec	OH VER Error	-999	06 07 --
NO_ver_unfilt(event, altitude)/f	ergs/cm^3/sec	NO VER	-999	06 07 20
NO_ver_top_unfilt(event, altitude)/f	ergs/cm^3/sec	NO VER	-999	06 07 20
NO_ver_unfilt_error(event, altitude)/f	ergs/cm^3/sec	NO VER Error	-999	06 07 --
NO_ver_top_unfilt_error(event, altitude)/f	ergs/cm^3/sec	NO VER Error	-999	06 07 --

* f=float, d=double, s=short, i=int, c=char.

** 06=1.06, 07=1.07, 20=2.0, RED means data unfilled for that version.

*** The 81-day average F10.7 flux is not available because the 81-day average is centered about the current day; while we could run on older data and have a value, processing of the newer data would have to be delayed until +40 days after the date of the data to permit the average value to be calculated. The daily flux value (limited to the range 71 - 212) is substituted for the average in the processing code.

Table A.3 describes the contents of the SABER L2B files. This table lists each variable contained in the netCDF file along with its type, dimensions, units, long name, and missing value. The variables that are dimensioned use the variables: Altitude = 400, Event = UNLIMITED, and Vector =3. The Event dimension will depend on the number of events in the netCDF file. Vector is used only for a lunar vector variable. The variables that have the _top in the name are for the top half of the altitude range (extending to about 285km). The same variable without the _top extension is for the bottom half of the altitude range (roughly 15km to 155km). Note that there are several versions of Level2B data, the column to the far right indicates for which versions (starting with 1.06) a particular variable is included.

Table A.3. Level 2B variables.

Variable(dimensions)/type*	units	Long name	Miss. value	Version**
event(event)/s		Event Number for Current File		06 07 20
date(event)/i	yyyyddd	Date [yyyyddd]	-999	06 07 20
mode(event)/s		0=Down 1=Up	-999	06 07 20
tpDN(event)/s		0=Day 1=Night 2=Twilight	-999	06 07 20
tpAD(event)/s		0=Ascending 1=Descending	-999	06 07 20
moonSepAngle(event)/f	degrees	Angle between moon and LOS	-999	06 07 20
tpaltmoonSepAngle(event)/f	km	Tpaltitude used for moonSepAngle	-999	06 07 20
solAP(event)/f		Solar Ap Index	-999	06 07 20
solKP(event)/f		Solar Kp Index	-999	06 07 20
solf10p7Daily(event)/f	10^{-22} W/m2/Hz	F10.7 Flux (Daily	-999	06 07 20
***solF10p781dAvg(event)/f	10^{-22} W/m2/Hz	F10.7 Flux (81-day Average)	-999	06 07 20
solSpotNo(event)/s		Zurich Sunspot Number	-999	06 07 20
scSolarZen(event)/f	degrees	Sc Solar-Zenith Angle	-999	06 07 20
earth_sun(event)/f	km	Earth-Sun Distance	-999	06 07 20

L1_altoff(event)/f	km	Altitude Offset from Level1	-999	-- -- 20
Iaurora(event)/s		Aurora Flag (1=TRUE, 0=FALSE)	-999	06 07 20
time(event,altitude)/i	msec	Msec Since Midnight	-999	06 07 20
sclatitude(event, altitude)/f	degrees	Spacecraft Latitude	-999	06 07 20
sclongitude(event, altitude)/f	degrees	Spacecraft Longitude	-999	06 07 20
scaltitude(event, altitude)/f	km	Spacecraft Altitude	-999	06 07 20
tpaltitude(event, altitude)/f	km	Tangent-Point Altitude	-999	06 07 20
tplatitude(event, altitude)/f	degrees	Tangent-Point Latitude	-999	06 07 20
tplongitude(event, altitude)/f	degrees	Tangent-Point Longitude	-999	06 07 20
tpSolarZen(event, altitude)/f	degrees	Tangent-Point Solar-Zenith Angle	-999	06 07 20
tpSolarLT(event, altitude)/f	msec	Tangent-Point Local-Solar Time	-999	06 07 20
elevation(event, altitude)/d	milliradians	Elevation Angle	-999	06 07 20
NO_cool(event, altitude)/f	K/day	cooling rate for NO	-999	06 07 --
CO2_cool_626_01101_00001(event, altitude)/f	K/day	cooling rate for CO2_626_01101_00001	-999	06 07 20
CO2_cool_626_02201_01101(event, altitude)/f	K/day	cooling rate for CO2_626_02201_01101	-999	06 07 20
CO2_cool_626_03301_02201(event, altitude)/f	K/day	cooling rate for CO2_626_03301_02201	-999	06 07 20
CO2_cool_626_00011_00001(event, altitude)/f	K/day	cooling rate for CO2_626_00011_00001	-999	06 07 20
CO2_cool_626_01111_01101(event, altitude)/f	K/day	cooling rate for CO2_626_01111_01101	-999	06 07 20
CO2_cool_626_10012_00001(event, altitude)/f	K/day	cooling rate for CO2_626_10012_00001	-999	06 07 20
CO2_cool_626_10011_00001(event, altitude)/f	K/day	cooling rate for CO2_626_10011_00001	-999	06 07 20
CO2_cool_626_10012_10002(event, altitude)/f	K/day	cooling rate for CO2_626_10012_10002	-999	06 07 20
CO2_cool_626_02211_02201(event, altitude)/f	K/day	cooling rate for CO2_626_02211_02201	-999	06 07 20
CO2_cool_626_10011_10001(event, altitude)/f	K/day	cooling rate for CO2_626_10011_10001	-999	06 07 20

CO2_cool_626_11112_01101(event, altitude)/f	K/day	cooling rate for CO2_626_11112_01101	-999	06 07 20
CO2_cool_626_11111_01101(event, altitude)/f	K/day	cooling rate for CO2_626_11111_01101	-999	06 07 20
CO2_cool_626_11112_11102(event, altitude)/f	K/day	cooling rate for CO2_626_11112_11102	-999	06 07 20
CO2_cool_626_03311_03301(event, altitude)/f	K/day	cooling rate for CO2_626_03311_03301	-999	06 07 20
CO2_cool_626_11111_11101(event, altitude)/f	K/day	cooling rate for CO2_626_11111_11101	-999	06 07 20
CO2_cool_626_20013_00001(event, altitude)/f	K/day	cooling rate for CO2_626_20013_00001	-999	06 07 20
CO2_cool_626_20012_00001(event, altitude)/f	K/day	cooling rate for CO2_626_20012_00001	-999	06 07 20
CO2_cool_626_20011_00001(event, altitude)/f	K/day	cooling rate for CO2_626_20011_00001	-999	06 07 20
CO2_cool_636_01101_00001(event, altitude)/f	K/day	cooling rate for CO2_636_01101_00001	-999	06 07 20
CO2_cool_636_02201_01101(event, altitude)/f	K/day	cooling rate for CO2_636_02201_01101	-999	06 07 20
CO2_cool_636_00011_00001(event, altitude)/f	K/day	cooling rate for CO2_636_00011_00001	-999	06 07 20
CO2_cool_628_01101_00001(event, altitude)/f	K/day	cooling rate for CO2_628_01101_00001	-999	06 07 20
CO2_cool_628_02201_01101(event, altitude)/f	K/day	cooling rate for CO2_628_02201_01101	-999	06 07 20
CO2_cool_628_00011_00001(event, altitude)/f	K/day	cooling rate for CO2_628_00011_00001	-999	06 07 20
CO2_cool_627_01101_00001(event, altitude)/f	K/day	cooling rate for CO2_627_01101_00001	-999	06 07 20
CO2_cool_627_02201_01101(event, altitude)/f	K/day	cooling rate for CO2_627_02201_01101	-999	06 07 20

CO2_cool_627_00011_00001(event, altitude)/f	K/day	cooling rate for CO2_627_00011_00001	-999	06 07 20
H2O_cool_161_010_000(event, altitude)/f	K/day	cooling rate for H2O_161_010_000	-999	06 07 20
H2O_cool_161_020_000(event, altitude)/f	K/day	cooling rate for H2O_161_020_000	-999	06 07 20
H2O_cool_161_020_010(event, altitude)/f	K/day	cooling rate for H2O_161_020_010	-999	06 07 20
H2O_cool_161_100_000(event, altitude)/f	K/day	cooling rate for H2O_161_100_000	-999	06 07 20
H2O_cool_161_100_010(event, altitude)/f	K/day	cooling rate for H2O_161_100_010	-999	06 07 20
H2O_cool_161_001_000(event, altitude)/f	K/day	cooling rate for H2O_161_001_00	-999	06 07 20
H2O_cool_161_001_010(event, altitude)/f	K/day	cooling rate for H2O_161_001_010	-999	06 07 20
H2O_cool_161_011_000(event, altitude)/f	K/day	cooling rate for H2O_161_011_000	-999	06 07 20
H2O_cool_farir(event,altitude)/f	K/day	cooling rate for H2O in the far-ir	-999	06 07 --
O3_cool_666_001_000(event, altitude)/f	K/day	cooling rate for O3_666_001_000	-999	06 07 20
O3_cool_666_010_000(event, altitude)/f	K/day	cooling rate for O3_666_010_000	-999	06 07 --
O3_cool_666_100_000(event, altitude)/f	K/day	cooling rate for O3_666_100_000	-999	06 07 --
O3_cool_666_011_001(event, altitude)/f	K/day	cooling rate for O3_666_011_001	-999	06 07 --
CO2_solar_heat_626_00011_00001(event, altitude)/f	K/day	solar_energy deposition rate for CO2_626_00011_00001	-999	06 07 --
CO2_solar_heat_626_01111_01101(event, altitude)/f	K/day	solar_energy deposition rate for CO2_626_01111_01101	-999	06 07 --
CO2_solar_heat_626_10012_00001(event, altitude)/f	K/day	solar_energy deposition rate for CO2_626_10012_00001	-999	06 07 --

CO2_solar_heat_626_10011_000 01(event, altitude)/f	K/day	solar_energy deposition rate for CO2_626_10011_00001	-999	06 07 --
CO2_solar_heat_626_10012_100 02(event, altitude)/f	K/day	solar_energy deposition rate for CO2_626_10012_10002	-999	06 07 --
CO2_solar_heat_626_02211_022 01(event, altitude)/f	K/day	solar_energy deposition rate for CO2_626_02211_02201	-999	06 07 --
CO2_solar_heat_626_10011_100 01(event, altitude)/f	K/day	solar_energy deposition rate for CO2_626_10011_10001	-999	06 07 --
CO2_solar_heat_626_11112_011 01(event, altitude)/f	K/day	solar_energy deposition rate for CO2_626_11112_01101	-999	06 07 --
CO2_solar_heat_626_11111_011 01(event, altitude)/f	K/day	solar_energy deposition rate for CO2_626_11111_01101	-999	06 07 --
CO2_solar_heat_626_11112_111 02(event, altitude)/f	K/day	solar_energy deposition rate for CO2_626_11112_11102	-999	06 07 --
CO2_solar_heat_626_03311_033 01(event, altitude)/f	K/day	solar_energy deposition rate for CO2_626_03311_03301	-999	06 07 --
CO2_solar_heat_626_11111_111 01(event, altitude)/f	K/day	solar_energy deposition rate for CO2_626_11111_11101	-999	06 07 --
CO2_solar_heat_626_20013_000 01(event, altitude)/f	K/day	solar_energy deposition rate for CO2_626_20013_00001	-999	06 07 --
CO2_solar_heat_626_20012_000 01(event, altitude)/f	K/day	solar_energy deposition rate for CO2_626_20012_00001	-999	06 07 --
CO2_solar_heat_626_20011_000 01(event, altitude)/f	K/day	solar_energy deposition rate for CO2_626_20011_00001	-999	06 07 --
CO2_solar_heat_636_00011_000 01(event, altitude)/f	K/day	solar_energy deposition rate for CO2_636_00011_00001	-999	06 07 --
CO2_solar_heat_628_00011_000 01(event, altitude)/f	K/day	solar_energy deposition rate for CO2_628_00011_00001	-999	06 07 --
CO2_solar_heat_627_00011_000 01(event, altitude)/f	K/day	solar_energy deposition rate for CO2_627_00011_00001	-999	06 07 --
H2O_solar_heat_161_010_000(e vent, altitude)/f	K/day	solar_energy deposition rate for H2O_161_010_000	-999	06 07 --

H2O_solar_heat_161_020_000(event, altitude)/f	K/day	solar_energy deposition rate for H2O_161_020_000	-999	06 07 --
H2O_solar_heat_161_020_010(event, altitude)/f	K/day	solar_energy deposition rate for H2O_161_020_010	-999	06 07 --
H2O_solar_heat_161_100_000(event, altitude)/f	K/day	solar_energy deposition rate for H2O_161_100_000	-999	06 07 --
H2O_solar_heat_161_100_010(event, altitude)/f	K/day	solar_energy deposition rate for H2O_161_100_010	-999	06 07 --
H2O_solar_heat_161_001_000(event, altitude)/f	K/day	solar_energy deposition rate for H2O_161_001_000"	-999	06 07 --
H2O_solar_heat_161_001_010(event, altitude)/f	K/day	solar_energy deposition rate for H2O_161_001_010	-999	06 07 --
H2O_solar_heat_161_011_000(event, altitude)/f	K/day	solar_energy deposition rate for H2O_161_011_000	-999	06 07 --
SJ_hartley(event, altitude)/f	/s	Photodissociation rate for O3_hartley	-999	-- -- 20
O3_solar_heat_hartley(event, altitude)/f	K/day	solar heating rate for O3_hartley	-999	06 07 20
O3_solar_heat_huggins(event, altitude)/f	K/day	solar heating rate for O3_huggins	-999	06 07 20
O3_solar_heat_chappuis(event, altitude)/f	K/day	solar heating rate for O3_chappuis	-999	06 07 20
O2_solar_heat_ly_alpha(event, altitude)/f	K/day	solar heating rate for O2_ly_alpha	-999	06 07 20
O2_solar_heat_herzberg(event, altitude)/f	K/day	solar heating rate for O2_herzberg	-999	06 07 20
O2_solar_heat_schumann_runge_cont(event, altitude)/f	K/day	solar heating rate for O2_schumann_runge_cont	-999	06 07 20
O2_solar_heat_schumann_runge_band(event, altitude)/f	K/day	solar heating rate for O2_schumann_runge_band	-999	06 07 20
O2_solar_heat_atmospheric_bands(event, altitude)/f	K/day	solar energy deposition rate O2_atmospheric_bands	-999	06 07 20
chem_heat_H_O2_M(event, altitude)/f	K/day	chemical heating rate for H+O2+M	-999	06 07 20

chem_heat_H_O3(event, altitude)/f	K/day	chemical heating rate for H+O3	-999	06 07 20
chem_heat_O_O3(event, altitude)/f	K/day	chemical heating rate for O+O3	-999	06 07 20
chem_heat_O_OH(event, altitude)/f	K/day	chemical heating rate for O+OH	-999	06 07 20
chem_heat_O_HO2(event, altitude)/f	K/day	chemical heating rate for O+HO2	-999	06 07 20
chem_heat_O_O_M(event, altitude)/f	K/day	chemical heating rate for O+O+M	-999	06 07 20
chem_heat_O_O2_M(event, altitude)/f	K/day	chemical heating rate for O+O2+M	-999	06 07 20

* f=float, d=double, s=short, i=int, c=char.

** 06=1.06, 07=1.07, 20=2.0, RED means data unfilled for that version.

*** The 81-day average F10.7 flux is not available because the 81-day average is centered about the current day; while we could run on older data and have a value, processing of the newer data would have to be delayed until +40 days after the date of the data to permit the average value to be calculated. The daily flux value (limited to the range 71 - 212) is substituted for the average in the processing code.

Appendix B - SABER Formal Publications in Archival Literature

Instrument Performance and Calibration

1. Mlynczak, M. G., et al. (2020), Radiometric stability of the SABER instrument, *Earth and Space Science*, https://doi.org/10.1029/2019EA001011.

2 Tansock, J. J., J. M. Russell III, M. G. Mlynczak, L. L. Gordley, C. Brown, G. Paxton, and P. McMichaels (2006), An update of sounding of the atmosphere using broadband emission radiometry (SABER) calibration, *Proc. SPIE*, 6297, 62970V, DOI:10.1117/12.692857.

3. Tansock, J. J., S. Hansen, K. Paskett, A. Shumway, J. Peterson, J. Stauder, L. Gordley, Y. Wang, M. Melbert, J. Russell, and M. G. Mlynczak (2003), SABER Ground Calibration, *Int. J. Remote Sens*., 24. 403-420.

4. Russell, J. M. III, M. G. Mlynczak, L. L. Gordley, J. J. Tansock, Jr., and R. W. Esplin (1999), Overview of the SABER experiment and preliminary calibration results, *Proc. SPIE*, 3756, 277, DOI:10.1117/12.366382.

5. Stauder, J. L., R. W. Esplin, L. Zollinger, M. G. Mlynczak, J. M. Russell III, L. L. Gordley, and B. T. Marshall (1995), Stray-light analysis of the SABER telescope, *Proc. SPIE*, 2553, 264, DOI:10.1117/12.221362.

6. Russell, J. M. III, M. G. Mlynczak, and L. L. Gordley (1994), Overview of the Sounding of the Atmosphere Using Broadband Emission Radiometry (SABER) experiment for the Thermosphere-Ionosphere-Mesosphere Energetics and Dynamics (TIMED) mission, *Proc. SPIE*, 2266, 406, DOI:10.1117/12.187579.

Kinetic Temperature and Carbon Dioxide

7. Rezac, L., Yue, J., Yongxiao, J., Russell, J. M. III, Garcia, R., Lopez-Puertas, M., and Mlynczak, M. G. (2018), On long-term SABER CO_2 trends and effects due to nonuniform space and time sampling, *Journal of Geophysical Research: Space Physics*, 123. https://doi.org/10.1029/2018JA025892.

8. Dawkins, E., A. Feofilov, L. Rezac, A. A. Kutepov, D. Janches, M. Mlynczak, and J. Russell (2017), Validation of SABER v2.0 operational temperature data with ground-based lidars: first results and justification of methodology, *J. Geophys. Res*., https://doi.org/10.1029/2018JD028742.

9. Yue, J., J. Russell III, Y. Jian, L. Rezac, R. Garcia, M. López-Puertas, *and* M. G. Mlynczak (2015), Increasing carbon dioxide concentration in the upper atmosphere observed by SABER, Geophys. Res. Lett., 42, 7194–7199, *doi:*10.1002/2015GL064696.

10. Rezac, L., Jian, Y., Yue, J., Russell, J. M., Kutepov, A., Garcia, R., et al. (2015), Validation of the global distribution of CO2 volume mixing ratio in the mesosphere and lower thermosphere from SABER, *Journal of Geophysical Research: Atmospheres*, 120, 12,067–12,081. https://doi.org/10.1002/2015JD023955.

11. Rezac, L., Kutepov, A., Russell, J. M., Feofilov, A. G., Yue, J., & Goldberg, R. A. (2015), Simultaneous retrieval of T(p) and CO2 VMR from two-channel non-LTE limb radiances and application to daytime SABER/TIMED measurements, *Journal of Atmospheric and Solar-Terrestrial Physics*, 130, 23–42. https://doi.org/10.1016/j.jastp.2015.05.004.

12. Smith, S. M., J. Baumgardner, C.J. Mertens, J.M. Russell, M.G. Mlynczak, M. Mendillo (2010), Mesospheric OH Temperatures: Simultaneous Ground-based and SABER OH Measurements over Millstone Hill, *Advances in Space Research*, 45, 239-246.

13. Mertens, C. J., J. M. Russell III, M. G. Mlynczak, C-Y She, F. J. Schmidlin, R. A. Goldberg, M. López-Puertas, P. P. Wintersteiner, R. H. Picard, J. R. Winick, X. Xu (2009), Kinetic temperature and carbon dioxide from broadband infrared limb emission measurements taken from the TIMED/SABER instrument, *Adv. Space Res*., 43, 1, 15-27.

14. Mertens, C. J., J. R. Winick, R. H. Picard, D. S. Evans, M. López-Puertas, P. P. Wintersteiner, X. Xu, M. G. Mlynczak, J. M. Russell III (2009), Influence of solar-geomagnetic disturbances on SABER measurements of 4.3 μm emission and the retrieval of kinetic temperature and carbon dioxide, *Adv. Space Res*., 43, 9, 1325-1336.

15. Mertens, C. J., J. R. Fernandez, X. Xu, D. S. Evans, M. G. Mlynczak, and J. M. Russell III (2008), A new source of auroral infrared emission observed by TIMED/SABER, *Geophys. Res. Lett*., 35, 17-20.

16. Remsberg, E. E., B. T. Marshall, M. Garcia-Comas, et al. (2008), Assessment of the quality of the retrieved temperature versus pressure profiles in the middle atmosphere from TIMED/SABER, *J. Geophys. Res*., 113, D17, doi:10.1029/2008JD010013.

17. Garcia-Comas, M., M. López-Puertas, B. T. Marshall, et al. (2008), Error in SABER temperature caused by non-LTE model parameters, *J. Geophys. Res*., 113, D24, doi:10.1029/2008JD010105.

18. Schwartz, M. et al. (2008), Validation of the Aura Microwave Limb Sounder Temperature and Geopotential Height Measurements, *J. Geophys. Res*., 113, D15, doi:10.1029/2007JD008783.

19. Wrasse, C. M., J. Fechine, H. Takahashi, C. M. Denardini, J. Wickert, M. G. Mlynczak, J. M. Russell and C. L. Barbosa (2008), Temperature comparison between CHAMP radio occultation and TIMED/SABER measurements in the lower stratosphere, *Adv. Space Res.*, 41, 1423-1428.

21. López-González, M. J., M. Garcia-Comas, E. Rodríguez, M. López-Puertas, M.G. Shepherd, G.G. Shepherd, S. Sargoytchev, V.M. Aushev, S.M. Smith, M. G. Mlynczak, J.M. Russell, S. Brown, Y.-M. Cho and R.H. Wiens (2007), Ground-based mesospheric temperatures at mid-latitude derived from O_2 and OH airglow SATI data: Comparison with SABER measurements, *J. Atmos. Sol-Terr. Phys*, 2379-2390.

22. Huang, F. T., H. Mayr, J. M. Russell III, M. G. Mlynczak, C. A. Reber, and J. G. Mengel (2007), Ozone quasi-biennial oscillations (QBO), semiannual oscillations (SAO), and correlations with temperature in the mesosphere, lower thermosphere, and stratosphere, based on measurements from SABER on TIMED and MLS on UARS, *J. Geophys. Res*., doi:10.1029/2007JA012634.

23. Oberheide J., D. Offermann, J. M. Russell III, M. G. Mlynczak (2006), Intercomparison of kinetic temperature from 15 mm CO_2 limb emissions and OH*(3,1) rotational temperature in nearly coincident air masses: SABER, GRIPS, *Geophys. Res. Lett*., 33, L14811, doi:10.1029/2006GL026439.

24. Huang F. T., H. G. Mayr, C. A. Reber, J. Russell, M. Mlynczak, J. Mengel (2006), Zonal-mean temperature variations inferred from SABER measurements on TIMED compared with UARS observations, *J. Geophys. Res*., 111, A10S07, doi:10.1029/2005JA011427.

25. Xu J., C. Y. She, W. Yuan, C. Mertens, M. Mlynczak, J. Russell (2006), Comparison between the temperature measurements by TIMED/SABER and lidar in the midlatitude, *J. Geophys. Res*., 111, A10S09, doi:10.1029/2005JA011439.

26. Mertens C. J., et al. (2004), SABER observations of mesospheric temperatures and comparisons with falling sphere measurements taken during the 2002 summer MaCWAVE campaign, *Geophys. Res. Lett*., 31, L03105, doi:10.1029/2003GL018605.

27. Wang, Ding-Yi, G. P. Stiller, T. von Clarmann, M. Garcia-Comas, M. López-Puertas, M. W. Kiefer, M. Hoepfner, N. Glatthor, B. Funke, S. Gil-Lopez, U. Grabowski, S. Kellmann, A. Linden, G. M. Tsidu, M. Milz, T. Steck, H. Fischer, J. M. Russell III, E. E. Remsberg, C. J. Mertens, and M. G. Mlynczak (2004), Comparisons of MIPAS-observed temperature profiles with other satellite measurements, *Proc. SPIE*, 5235, 196, DOI:10.1117/12.514244.

28. Gordley, L. L., B. T. Marshall, Steven B. Jacobson, Martin G. Mlynczak, and James M. Russell III (2004), Rapid non-LTE analysis of CO_2 limb emission from the upper mesosphere to obtain kinetic temperature and pressure, *Proc. SPIE*, 5235, 240, DOI:10.1117/12.514390.

29. López-Puertas M., M. Garcia-Comas, B. Funke, R. H. Picard, J. R. Winick, P. P. Wintersteiner, M. G. Mlynczak, C. J. Mertens, J. M. Russell III, L. L. Gordley (2004), Evidence for an OH(v) excitation mechanism of CO_2 4.3 μm nighttime emission from SABER/TIMED measurements, *J. Geophys. Res.,* 109, D09307, doi:10.1029/2003JD004383.

30. Remsberg E., G. Lingenfelser, V. L. Harvey, W. Grose, J. Russell III, M. Mlynczak, L. Gordley, B. T. Marshall (2003), On the verification of the quality of SABER temperature, geopotential height, and wind fields by comparison with Met Office assimilated analyses, *J. Geophys. Res*., 108 (D20), 4628, doi:10.1029/2003JD003720.

31. Mertens, C. J., M. G. Mlynczak, M. Lopez-Puertas, P. P. Wintersteiner, R. H. Picard, J. R. Winick, L. L. Gordley, and J. M. Russell III (2001), Retrieval of mesospheric and lower thermospheric kinetic temperature from measurements of CO_2 15 μm Earth limb emission under non-LTE conditions, *Geophys. Res. Lett*., 28(7), 1391-1394.

Ozone (9.6 μm)

32. Smith, A. K., V. L. Harvey, M. G. Mlynczak, M. Garcıa-Comas, M. Kaufmann, E. Kyrola, M. Lopez-Puertas, I. McDade, C. E. Randall, J. M. Russell III, P. E. Sheese, M. Shiotani, W. R. Skinner, M Suzuki, K. A. Walker (2013), Satellite Observations of Ozone in the Upper Mesosphere, *J. Geophys. Res*., DOI:10.1002/jgrd.50445.

33. Imai, K., et al., (2013), Validation of ozone data from the superconducting submillimeter-wave limb emission sounder (SMILES), *J. Geophys. Res*., DOI:10.1002/jgrd.50434.

34. Mieruch, S., M. Weber, C. von Savigny, A. Rozanov, H. Bovensmann, J. P. Burrows, P. F. Bernath, C. D. Boone, L. Froidevaux, L. L. Gordley, M. G. Mlynczak, J. M. Russell III, L. W. Thomason, K. A. Walker, and J. M. Zawodny (2012), Global and long-term comparison of SCIAMACHY limb ozone profiles with correlative satellite data (2002–2008), *Atmos. Meas. Tech*., 5, 771-788, doi:10.5194/amt-5-771-2012.

35. Rong P. P., J. M. Russell III, M. G. Mlynczak, E. E. Remsberg, B. T. Marshall, L. L. Gordley, M. López-Puertas (2009), Validation of Thermosphere Ionosphere Mesosphere Energetics and Dynamics/Sounding of the Atmosphere using Broadband Emission Radiometry (TIMED/SABER) v1.07 ozone at 9.6 μm in altitude range 15–70 km, *J. Geophys. Res*., 114, D04306, doi:10.1029/2008JD010073.

36. Huang, F. T., H. G. Mayr, C. A. Reber, J. M Russell, III, M. G. Mlynczak, and J. G. Mengel (2008), Ozone quasi-biennial oscillations (QBO), semiannual oscillations (SAO), and correlations with temperature in the mesosphere, lower thermosphere, and stratosphere, based on measurements from SABER on TIMED and MLS on UARS, *J. Geophys. Res*., 113, A01316, doi:10.1029/2007JA012634.

37. Zhou, D. K., M. G. Mlynczak, G. E. Bingham, J. O. Wise, R. M. Nadile (1998), CIRRIS-1A limb spectral measurements of mesospheric 9.6 μm airglow and ozone, *Geophys. Res. Lett*., 25(5), 643-646, 10.1029/98GL00236.

38. Mlynczak, M. G., D. K. Zhou (1998), Kinetic and spectroscopic requirements for the measurement of mesospheric ozone at 9.6 μm under non-LTE conditions, *Geophys. Res. Lett*., 25(5), 639-642, 10.1029/98GL00092.

39. Edwards, D. P., J. B. Kumer, M. López-Puertas, M. G. Mlynczak, A. Gopalan, J. C. Gille, A. Roche (1996), Non-local thermodynamic equilibrium limb radiance near 10 μm as measured by UARS CLAES, *J. Geophys. Res*., 101(D21), 26577-26588, 10.1029/96JD02133.

40. Edwards, D. P., Manuel López-Puertas and Martin G. Mlynczak (1994), Non-local thermodynamic equilibrium limb radiance from O_3 and CO_2 in the 9–11 μ m spectral region, *Journal of Quantitative Spectroscopy and Radiative Transfer*, Volume 52, Issues 3-4, September-October 1994, Pages 389-407.

41. Mlynczak, M. G., and S. Roland Drayson (1991), Rapid computation of the radiative absorption rate in the v_3 mode of mesospheric and lower thermospheric ozone, *Journal of Quantitative Spectroscopy and Radiative Transfer*, Volume 46, Issue 5, November 1991, Pages 463-471.

42. Mlynczak, M. G., S. R. Drayson (1990), Calculation of infrared limb emission by ozone in the terrestrial middle atmosphere. 1. Source functions, *J. Geophys. Res*., 95(D10), 16497-16511, 10.1029/90JD01306.

43. Mlynczak, M. G., S. R. Drayson (1990), Calculation of infrared limb emission by ozone in the terrestrial middle atmosphere. 2. Emission calculations, *J. Geophys. Res*., 95(D10), 16513-16521, 10.1029/90JD01307.

Ozone (1.27 μm, day only)

44. Dikty, S., H. Schmidt, M. Weber, C. von Savigny, and M. G. Mlynczak (2010), Daytime ozone and temperature variations in the mesosphere: a comparison between SABER observations and HAMMONIA model, *Atmos. Chem. Phys*., 10, 8331-8339, doi:10.5194/acp-10-8331-2010.

45. Mlynczak M. G., B. T. Marshall, F. J. Martin-Torres, J. M. Russell III, R. E. Thompson, E. E. Remsberg, L. L. Gordley (2007), Sounding of the Atmosphere using Broadband Emission Radiometry observations of daytime mesospheric $O_2(^1\Delta)$ 1.27 μ m emission and derivation of ozone, atomic oxygen, and solar and chemical energy deposition rates, *J. Geophys. Res*., 112, D15306, doi:10.1029/2006JD008355.

46. Mlynczak, M. G., F. Morgan, J.-H. Yee, P. Espy, D. Murtagh, B. Marshall, F. Schmidlin (2001), Simultaneous measurements of the $O_2(^1\Delta)$ and $O_2(^1\Sigma)$ airglows and ozone in the daytime mesosphere, *Geophys. Res. Lett*., 28(6), 999-1002, 10.1029/2000GL012423.

47. Mlynczak, M. G., R. R. Garcia, R. G. Roble, M. Hagan (2000), Solar energy deposition rates in the mesosphere derived from airglow measurements: Implications for the ozone model deficit problem, *J. Geophys. Res*., 105(D13), 17527-17538, 10.1029/2000JD900222.

48. Mlynczak, M. G., D. J. Nesbitt (1995), The Einstein coefficient for spontaneous emission of the $O_2(^1\Delta)$ state, *Geophys. Res. Lett*., 22(11), 1381-1384, 10.1029/95GL01320.

49. Mlynczak, M. G., D. S. Olander (1995), On the utility of the molecular oxygen dayglow emissions as proxies for middle atmospheric ozone, *Geophys. Res. Lett*., 22(11), 1377-1380, 10.1029/95GL01321.

50. Mlynczak, M. G. (1993), An evaluation of the rate of absorption of solar radiation in the $O_2(^3\Sigma \rightarrow {}^1\Sigma)$ transition, *Geophys. Res. Lett*., 20(14), 1439-1442, 10.1029/93GL01457.

51. Mlynczak, M. G., S. Solomon, D. S. Zaras (1993), An updated model for $O_2(^1\Delta)$ concentrations in the mesosphere and lower thermosphere and implications for remote sensing of ozone at 1.27 μm, *J. Geophys. Res*., 98(D10), 18639-18648, 10.1029/93JD01478.

Water Vapor

52. Yue, J., Russell, J., Gan, Q., Wang, T., Rong, P., Garcia, R., & Mlynczak, M. (2019). Increasing Water Vapor in the Stratosphere and Mesosphere After 2002. *Geophysical Research Letters*, 46. https://doi.org/10.1029/2019GL084973.

53. Rong, P. P., J. M. Russell, B. T. Marshall, L. L. Gordley, M. G. Mlynczak, and K. A. Walker (2019). Validation of water vapor measured by SABER on the TIMED satellite, *J. Atmos. Sol. Terr. Phys*., https://doi.org/10.1016/j.jastp.2019.105099.

54. Zhou, D. K., M. G. Mlynczak, M. López-Puertas, G. Zaragoza (1999), Evidence of non-LTE effects in mesospheric water vapor from spectrally resolved emissions observed by CIRRIS-1A, *Geophys. Res. Lett*., 26(1), 67-70, 10.1029/1998GL900233.

55. Mertens C. J., M. G. Mlynczak, M. Lopez-Puertas, and E. E. Remsberg (2002), Impact of non-LTE processes on middle atmospheric water vapor retrievals from simulated measurements of 6.8 μm Earth limb emission, *Geophys. Res. Lett*., 29 (9), doi:10.1029/2001GL014590.

56. Mlynczak, M. G. (1999), Kinetic requirements for the measurement of mesospheric water vapor at 6.8 μm under non-LTE conditions, *Geophys. Res. Lett*., 26(1), 63-66, 10.1029/1998GL900232, 1999.

Atomic oxygen

57. Lednyts'kyy, O., C. von Savigny, Miriam Sinnhuber, N. Iwagami, M. Mlynczak (2019), Multiple airglow chemistry approach for atomic oxygen retrievals on the basis of in-situ nightglow emissions, *J. Atmos. Sol. Terr. Phys*., 194, https://doi.org/10.1016/j.jastp.2019.105096.

58. Fytterer, T., C. von Savigny, M. G. Mlynczak, and M. Sinnhuber (2019), Model results of OH airglow considering four different wavelength regions to derive night-time atomic oxygen and atomic hydrogen in the mesopause region, *Atmos. Chem. Phys*., https://www.atmos-chem-phys.net/19/1835/2019/.

59. Panka, P. A., Kutepov, A. A., Rezac, L., Kalogerakis, K. S., Feofilov, A. G., Marsh, D., et al. (2018), Atomic oxygen retrieved from the SABER 2.0- and 1.6-μm radiances using new first-principles nighttime OH(*v*) model, *Geophysical Research Letters*, 45, 5798– 5803. https://doi.org/10.1029/2018GL077677.

60. Mlynczak, M. G., L. A. Hunt, J. M. Russell, and B. T. Marshall (2018), Updated SABER Night Atomic Oxygen and Implications for SABER Ozone and Atomic Hydrogen, *Geophys. Res. Lett*., https://doi.org/10.1029/2018GL077377.

61. Panka, P., et al. (2017), Resolving the mesospheric nighttime 4.3 μm emission puzzle: Comparison of the $CO_2(\nu_3)$ and OH(ν) emission models, *Atmos. Chem. Phys*., 17, 9751–9760, https://doi.org/10.5194/acp-17-9751-2017.

62. Lednyts'kyy, C. von Savigny, K. U. Eichmann, and M. G. Mlynczak (2015), Atomic oxygen retrievals in the MLT region from SCIAMACHY nightglow limb measurements, *Atm. Meas. Tech*., 8, 1021-1041. doi: 10.5194/amt-8-1021-2015.

63. Mlynczak, M. G., et al. (2013), Radiative constraints on the minimum atomic oxygen concentration in the mesopause region, *Geophys Res. Lett*., 40, 3777–3780, doi:10.1002/grl.50725.

64. Mlynczak, M. G., et al. (2013), Radiative and energetic constraints on the global annual mean atomic oxygen concentration in the mesopause region, *J. Geophys. Res*., DOI: 10.1002/jgrd.50400.

65. Mlynczak, M. G. et al. (2013), Atomic oxygen in the mesosphere and lower thermosphere derived from SABER: Algorithm theoretical basis and measurement uncertainty, *J. Geophys. Res*., DOI: 10.1002/jgrd.50401.

Atomic hydrogen

66. Qian, L., Burns, A. G., Solomon, S. S., Smith, A. K., McInerney, J., Hunt, L., Marsh, D., Liu, H., Mlynczak, M. & Vitt, F. (2018). Temporal Variability of Atomic Hydrogen from the Mesopause to the Upper Thermosphere. *Journal of Geophysical Research: Space Physics,* 123. https://doi.org/10.1002/2017JA024998.

67. Mlynczak, M. G., et al., (2013), Atomic hydrogen in the mesopause region observed by SABER, *J. Geophys. Res*., DOI: 10.1002/2013JD021263.

Energetics parameters

68. Mlynczak, M. G., Hunt, L. A., Lopez-Puertas, M., Funke, B., Emmert, J., Solomon, S., … Mertens, C. (2021), Spectroscopy, gas kinetics, and opacity of thermospheric nitric oxide and implications for analysis of SABER infrared emission measurements at 5.3 μm, *J. Quant. Spectrosc. Radiat. Transfer*, 268, 107609. doi:10.1016/j.jqsrt.2021.107609

69. Mlynczak, M. G., L. A. Hunt, J. Russell, and B. T. Marshall (2018), Thermosphere Climate Indexes: Percentile Ranges and Adjectival Descriptors, *J. Atm. Solar-Terr. Phys*., https://doi.org/10.1016/j.jastp.2018.04.004.

70. Smith, A. K., M. López-Puertas, J. Xu, *and* M. G. Mlynczak (2015), The heating efficiency of the exothermic reaction $H + O_3$ in the mesosphere, J. Geophys. Res. Atmos., 120, 12739–12747, *doi:*10.1002/2015JD024061.

71. Mast, J., M. G. Mlynczak, L. A. Hunt, B. T. Marshall, C. J. Mertens, J. M. Russell III, R. E. Thompson, and L. L. Gordley, (2013) Absolute concentrations of highly vibrationally excited OH(v= 9 + 8) in the mesopause region derived from the TIMED/SABER instrument, *Geophys. Res. Lett*., DOI: 10.1002/grl.50167.

72. Mlynczak M. G., F. J. Martin-Torres, J. M. Russell III (2007), Correction to "Energy transport in the thermosphere during the solar storms of April 2002", *J. Geophys. Res*., 112, A02303, doi:10.1029/2006JA012008.

73. Gardner J. L., B. Funke, M. G. Mlynczak, M. López-Puertas, F. J. Martin-Torres, J. M. Russell III, S. M. Miller, R. D. Sharma, J. R. Winick (2007), Comparison of nighttime nitric oxide 5.3 μ m emissions in the thermosphere measured by MIPAS and SABER, *J. Geophys. Res*., 112, A10301, doi:10.1029/2006JA011984.

74. Mlynczak M. G., et al. (2005), Energy transport in the thermosphere during the solar storms of April 2002, *J. Geophys. Res*., 110, A12S25, doi:10.1029/2005JA011141.

75. Mlynczak M., et al. (2003), The natural thermostat of nitric oxide emission at 5.3 μm in the thermosphere observed during the solar storms of April 2002, *Geophys. Res. Lett*., 30 (21), 2100, doi:10.1029/2003GL017693.

76. Mlynczak, M. G. (2000), A contemporary assessment of the middle atmosphere energy budget, in Atmospheric Science Across the Stratopause, edited by D. Siskind, S. Eckermann, and M. Summers, *Geophysical Monographs Series 123*, American Geophysical Union, p. 37-52.

77. Mlynczak, M. G. (1999), A new perspective on the molecular oxygen and hydroxyl airglow emissions, *J. Geophys. Res*., 104(D22), 27535-27544, 10.1029/1999JD900839.

78. Mlynczak, M. G., D. K. Zhou, S. M. Adler-Golden (1998), Kinetic and spectroscopic requirements for the inference of chemical heating rates and atomic hydrogen densities from OH Meinel band measurements, *Geophys. Res. Lett*., 25(5), 647-650, 10.1029/98GL00325.

79. Mlynczak, M. G., B. T. Marshall (1996), A reexamination of the role of solar heating in the O_2 atmospheric and infrared atmospheric bands, *Geophys. Res. Lett*., 23(6), 657-660, 10.1029/96GL00145.

80. Meriwether, J. W., M. G. Mlynczak (1995), Is chemical heating a major cause of the mesosphere inversion layer?, *J. Geophys. Res*., 100(D1), 1379-1388, 10.1029/94JD01736.

81. Mlynczak, M. G., S. Solomon (1993), A detailed evaluation of the heating efficiency in the middle atmosphere, *J. Geophys. Res*., 98(D6), 10517-10541, 10.1029/93JD00315.

82. Mlynczak, M. G., S. Solomon (1991), Middle atmosphere heating by exothermic chemical reactions involving odd-hydrogen species, *Geophys. Res. Lett*., 18(1), 37-40, 10.1029/90GL02672.

83. Mlynczak, M. G., S. Solomon (1991), On the efficiency of solar heating in the middle atmosphere, *Geophys. Res. Lett*., 18(7), 1201-1204, 10.1029/91GL01525.

84. Mlynczak, M. G. (1991), Nonlocal thermodynamic equilibrium processes in ozone: Implications for the energy budget of the mesosphere and lower thermosphere, *J. Geophys. Res*., 96(D9), 17217-17228, 10.1029/91JD01833.

Radiative Transfer Techniques used in Operational Algorithms

85. Mlynczak, M. G., C. J. Mertens, R. R. Garcia, R. W. Portmann (1999), A detailed evaluation of the stratospheric heat budget 2. Global radiation balance and diabatic circulations, *J. Geophys. Res*., 104(D6), 6039-6066, 10.1029/1998JD200099.

86. Mertens, C. J., M. G. Mlynczak, R. R. Garcia, R. W. Portmann (1999), A detailed evaluation of the stratospheric heat budget 1. Radiation transfer, *J. Geophys. Res*., 104(D6), 6021-6038, 10.1029/1998JD200100.

87. Mlynczak, M. G., D. S. Olander, M. Lopez-Puertas (1994), Rapid computation of spectrally integrated non-local thermodynamic equilibrium limb emission, *J. Geophys. Res*., 99(D12), 25761-25772, 10.1029/94JD02397.

88. Mlynczak, M. G., D. S. Olander, M. Lopez-Puertas, J. M. Russell III, and L. L. Gordley (1994), Rapid computation of spectrally integrated non-LTE limb emission, Proc. SPIE 2266, 425, DOI:10.1117/12.187581.

89. Marshall, B. T., L. L. Gordley, and D. A. Chu (1994), Bandpak: algorithms for modeling broadband transmission and radiance, J. Quant. Spectrosc. Radiat. Transfer, 52, 581-599.

90. Gordley, L. L., B. T. Marshall, and D. A. Chu (1994), LINEPAK: algorithms for modeling spectral transmittance and radiance, J. Quant. Spectrosc. Radiat. Transfer., 52, 563-580.

Mission Description

91. Mlynczak, M. G. (1997), Energetics of the mesosphere and lower thermosphere and the SABER experiment, *Advances in Space Research*, Volume 20, Issue 6, Pages 1177-1183.

92. Mlynczak, M. G. (1996), Energetics of the middle atmosphere: Theory and observation requirements, *Advances in Space Research,* Volume 17, Issue 11, Pages 117-126.

Other Publications: Includes Heritage, Ancillary data, Spectroscopy, etc.

93. Adler-Golden, S. M., M. W. Matthew, and D.R. Smith (1991), Upper atmospheric infrared radiance from CO2 and NO observed during the SPIRIT I Rocket Experiment*, J. Geophys. Res., 9*6, 11019-11648.

94. Barkstrom, B. R., G. L. Smith (1986), The Earth Radiation Budget Experiment: Science and Implementation, *Reviews of Geophysics*, Vol. 24, Issue 2, 379-390, doi:10.1029/RG024i002p00379.

95. Curtis, A.R. (1956), The computation of radiative heating rates in the atmosphere, *Proc. R. Soc*., A236, 156.

96. Edwards, D. P., M. López-Puertas, and M. A. López-Valverde (1993), Non-local thermodynamic equilibrium studies of the 15-μm bands of CO2 for atmospheric remote sensing, *J. Geophys. Res*.,98(D8), 14955–14977, doi:10.1029/93JD01297.

97. Feofilov, A. G., Kutepov, A. A., Pesnell, W. D., Goldberg, R. A., Marshall, B. T., Gordley, L. L., García-Comas, M., López-Puertas, M., Manuilova, R. O., Yankovsky, V. A., Petelina, S. V., and Russell III, J. M. (2009), Daytime SABER/TIMED observations of water vapor in the mesosphere: retrieval approach and first results, *Atmos. Chem. Phys*., 9, 8139-8158, doi:10.5194/acp-9-8139-2009.

98. Garcia, R. R., D. R. Marsh, D. E. Kinnison, B. A. Boville, and F. Sassi (2007), Simulations of secular trends in the middle atmosphere, 1950-2003, *J. Geophys. Res*., 112, D09301, doi:10.1029/2006JD007485.

99. Gille, J. C., and F. B. House (1971), On the inversion of limb radiance measurements, I, temperature and thickness, *J. Atmos. Sci*., 28, 1427-1442.

100. Gille, J. C., and P. L. Bailey (1978), Information content and results of non-linear inversion of Nimbus 6 Limb Radiance Inversion Radiometer data, Remote Sensing of the Atmosphere: Inversion Methods and Applications, edited by A. L. Fymat and V. E. Zuev, 107-113, Elsevier, New York, 1978.

101. Gille, J. C., and J. M. Russell III (1984), The Limb Infrared Monitor of the Stratosphere: Experiment Description, Performance, and Results, *J. Geophys. Res*., 89, 5125-5140.

102. Gille, J. C., et al. (1984), Validation of the temperature retrievals obtained by the Limb Infrared Monitor of the Stratosphere (LIMS) experiment on NIMBUS 7*, J. Geophys. Re*s., *89,* 5147-5160.

103. Gille, J. C., et al. (1984), Accuracy and precision of the nitric acid concentrations determined by the Limb Infrared Monitor of the Stratosphere experiment on NIMBUS 7, *J. Geophys. Res., 89,* 5179-5190.

104. Gordley, L. L., and J. M. Russell III (1981), Rapid inversion of limb radiance data using an emissivity growth approximation. *Appl. Opt.*, 20, 807.

105. Gordley, L. L., M. E. Hervig, C. Fish, J. M. Russell III, S. Bailey, J. Cook, S. Hansen, A. Shumway, G. J. Paxton, L. E. Deaver, B. T. Marshall, J. C. Burton, B. Magill, C. Brown, R. E. Thompson, and J. Kemp (2009), The solar occultation for ice experiment, *J. Atmos. Sol.-Terr. Phy*., 71(3–4), 300–315.

106. Kutepov, A. A., A. G. Feofilov, B. T. Marshall, L. L. Gordley, W. D. Pesnell, R. A. Goldberg, and J. M. Russell III (2006), SABER temperature observations in the summer polar mesosphere and lower thermosphere: importance of accounting for the CO_2 ν_2 quanta V-V exchange, *Geophys. Res. Lett.*, 33, L21809, doi:10.1029/2006GL026591.

107. Lopez-Puertas, M., R. Rodrigo, A. Molina, and F. W. Taylor (1986), A non-LTE transfer model for infrared bands in the middle atmosphere. I. Theoretical basis and application to CO2 15 μm bands, *J. Atmos. Terr. Phys*., 48, 729-748.

108. Lopez-Puertas, M., G. Zaragoza, M. A. Lopez-Valverde, and F. W. Taylor (1998), Non local thermodynamic equilibrium (LTE) atmospheric limb emission at 4.6 μm 1. An update of the CO2 non-LTE radiative transfer model, *J. Geophys. Res*., 103, 8499-8513.

109. Lopez-Puertas, M. and F.W. Taylor (2001), Non-LTE Radiative Transfer in the Atmosphere, Vol 3 of the Series on Atmospheric, Oceanic, and Planetary Physics, World Scientific Press, 2001, 487 pages, ISBN: 9812811494, 9789812811493.

110. Nadile, R. M., et al. (1991), Observations of infrared atmospheric emissions with the Cryogenic Infrared Radiance Instrumentation for Shuttle (CIRRUS 1A) from STS-39, EOS Transactions of the AGU, Fall Mtg. 1991, p.357.

111. Niro, F., T. von Clarmann, K. Jucks, and J-M. Hartmann (2005), Spectra calculations in central and wing regions of CO_2 IR bands between 10 and 20 μm, III: atmospheric emission spectra, *J. Quant. Spectrosc. Radiat. Transfer*, 92, 61-76.

112. Remsberg E. E., et al. (1984), The validation of NIMBUS 7 LIMS measurements of ozone*, J. Geophys. Res., 8*9, 5161-5178.

113. Remsberg, E. E., L. L. Gordley, B. T. Marshall, R. E. Thompson, J. Burton, P. Bhatt, V. L. Harvey, G. S. Lingenfelser, and M. Natarajan (2004), The Nimbus 7 LIMS Version 6 radiance conditioning and temperature retrieval methods and results, *J. Quant. Spectros. Rad. Transf*., vol. 86/4, 395-424, doi:10.1016/j.jqsrt.2003.12.007.

114. Roche, A. E., J. B. Kumer, J. L. Mergenthaler, G. A. Ely, W. G. Uplinger, J. F. Potter, T. C. James, and L. W. Sterritt (1993), The Cryogenic Limb Array Etalon Spectrometer (CLAES) on UARS: Experiment Description and Performance, *J. Geophys. Res*., 98, p10763-10775.

115. Rodgers, C. D., R. L. Jones, and J. J. Barnett (1984), Retrieval of temperature and composition from Nimbus 7 SAMS measurements, *J. Geophys. Res., 89,* 5280-5286.

116. Rodgers, C. D. (2000), Inverse Methods for Atmospheric Sounding: Theory and Practice, World Scientific Publishing Co. Ltd., 2000.

117. Rothman, L. S., et al. (2003), The HITRAN molecular spectroscopic database: edition of 2000 including updates through 2001, *J. Quant. Spectrosc. Radiat. Transfer*, 82, 5-44.

118. Russell III, James M., S. Roland Drayson (1972), The Inference of Atmospheric Ozone Using Satellite Horizon Measurements in the 1042 cm^{-1} Band. *J. Atmos. Sci.*, **29**, 376–390.

119. Russell, J. M. III et al. (1984), Validation of water vapor results measured by the Limb Infrared Monitor of the Stratosphere Experiment on NIMBUS 7*, J. Geophys., Res., 8*9, 5115-5124.

120. Russell, J. M. II, et al. (1984), Validation of nitrogen dioxide results measured by the Limb Infrared Monitor of the Stratosphere (LIMS) Experiment on NIMBUS 7, *J. Geophys. Res., 8*9, 5099 5108.

121. Russell III, J. M., L. L. Gordley, J. H. Park, S. R. Drayson, W. D. Hesketh, R. J. Cicerone, A. F. Tuck, J. E. Frederick, J. E. Harries, and P. J. Crutzen (1993), The halogen occultation experiment, *J. Geophys. Res*., 98, 10777–10797.

122. Solomon, S., J. T. Kiehl, B. J. Kerridge, E. E. Remsberg, and J. M. Russell III (1986), Evidence for nonlocal thermodynamic equilibrium in the ν3 mode of mesospheric ozone, *J. Geophys. Res*., 91, 9865–9876.

123. Stair, A. T. Jr. et al. (1983), The rocket borne cryogenic (10K) high resolution interferometer spectrometer flight- HIRIS: Atmospheric and auroral infrared emission spectra, *J. Appl. Optics, 22*, 1056.

124. Stair, A. T. Jr., et al. (1990), Observations of limb radiances with the cryogenic spectral infrared rocket experiment (SPIRE), *J. Geophys. Res., 90,* 9736-9775, 1985. Sun, C.-R. and C. B. Leovy, Ozone variability in the equatorial middle atmosphere, *J. Geophys. Res., 95*, 13829-13850.

125. Thomas, R. J., C. A. Barth, D. W. Rusch, and R. W. Sanders (1984), Solar Mesosphere Explorer near-infrared spectrometer: Measurements of 1.27 μm radiances and the inference of mesospheric ozone, *J. Geophys. Res*., 89, 9569–9580.

126. Wintersteiner, P. P., R. H. Picard, R. D. Sharma, J. R. Winick, R. A. Joseph (1992), Line by-line radiative excitation model for the non-equilibrium atmosphere - Application to CO2 15-microns emission, *J. Geophys. Res*., 97, 18083-18117.